University of Arkansas, Fayetteville
ScholarWorks@UARK

Theses and Dissertations

5-2020

An Evaluation of Unmanned Aircraft Systems' Ability to Assess Stripe Rust in Large Wheat Breeding Nursies

Jamison T. Murry
University of Arkansas, Fayetteville

Follow this and additional works at: https://scholarworks.uark.edu/etd

 Part of the Agronomy and Crop Sciences Commons, Plant Breeding and Genetics Commons, Plant Pathology Commons, and the Remote Sensing Commons

Citation

Murry, J. T. (2020). An Evaluation of Unmanned Aircraft Systems' Ability to Assess Stripe Rust in Large Wheat Breeding Nursies. *Theses and Dissertations* Retrieved from https://scholarworks.uark.edu/etd/3564

This Thesis is brought to you for free and open access by ScholarWorks@UARK. It has been accepted for inclusion in Theses and Dissertations by an authorized administrator of ScholarWorks@UARK. For more information, please contact ccmiddle@uark.edu.

An Evaluation of Unmanned Aircraft Systems'
Ability to Assess Stripe Rust in a Large Wheat Breeding Nurseries

A thesis submitted in partial fulfillment
of the requirements for the degree of
Master of Science in Crop, Soil, and Environmental Sciences

by

Jamison Murry
University of Arkansas at Pine Bluff
Bachelor of Science in Agronomy, 2017

May 2020
University of Arkansas

This thesis is approved from recommendation to the Graduate Council

_____
Richard Esten Mason, Ph.D.
Dissertation Director

_____
Leandro Mozzoni, Ph.D.
Committee Member

_____
Larry Purcell, Ph.D.
Committee Member

_____
Lisa Wood, Ph.D.
Committee Member

_____
John Rupe, Ph.D.
Committee Member

ABSTRACT

Stripe Rust (*Puccinia striiformis f. sp. tritici)* is a foliar disease that significantly impacts global wheat production, and resistant cultivars provide the most efficient method of control. High-throughput phenotyping using unmanned aircraft systems (UAS) offers a potentially more efficient method for field-based phenotyping compared to visual assessment. Here we tested the ability of remote sensing to predict stripe rust severity in a diverse population of 594 soft red winter wheat lines, planted in single-rows, and evaluated them by visually rating stripe rust intensity and remotely using the dark green color index (DGCI), normalized difference vegetation index (NDVI) and blue NDVI. Significant relationships ($p<0.0001$) were found between the visual and remote sensing data; however, the ability to predict severity is not accurate at the time. A genome-wide association study identified peaks on chromosomes 1B, 2A and 4B that were consistent between visual and DGCI and consistent with the location of known stripe rust resistance genes.

In a second study, the effect of plot size (single-row, two-row and four-row) on relationship between visual and remote sensing data (DGCI and NDVI) was explored. We evaluated a panel of 13 genotypes preselected to range from 0 to 100% severity, planted in three plot sizes across two measurement days. Significant ($p<0.0001$) relationships were observed between visual severity and remote sensing data with four-row plot sizes, generally indicating the strongest relationship, followed by two-row, with both being significantly greater than the single-row plot size. Overall this research will aid in the future implementation of remote sensing as a surrogate for visual rating of stripe rust severity.

©2020 by Jamison Murry
All Rights Reserved

ACKNOWLEDGMENT

I would like to express my gratitude to Dr. Esten Mason, my academic advisor, for his leadership motivation, patience, and enthusiasm that he has shown throughout the duration of this educational milestone. I would also like to thank my committee members, Dr. Larry Purcell, Dr. Lisa Wood, Dr. Leandro Mozzoni, and Dr. John Rupe for rendering their advice, expertise, and resources for this research. I would also like to thank Dr. Jason Tullis, the Department of Geosciences, and the Center for Advances Spatial Technologies, along with Dr. Edward Gbur and Mr. Kevin Thompson of the Agricultural Statistics laboratory for their support and expertise.

I am very grateful for my fellows of the Wheat Breeding and Genetics Lab. You all took me under your wings, gave me encouraging words and taught me more than any lecture I have ever sat in. The fun memories of collaborative field and lab work will last forever. I wish you all great success in your endeavors

Lastly, I want to thank my family, my friends and loved ones for all your undying support, fervent prayers and amazing love, while I was away pursuing my master's degree. To Miss. Kendyl Chanel Washington, I especially thank you for the love, support, and sacrifice that you have given and made for me to make this journey easier.

DEDICATION

To the incredible patriarch James Murry and phenomenal matriarchs of my family, the late Pearlie Horton, the late Emma Pickens, Doris Holmes, Dorothy Murry, and Joyce Murry. Your presence, prayers, leadership and experience, have been the catalyst that pushes me to overcome any obstacle on this road to success. I stand tall because I am on your shoulders, and I am eternally grateful.

TABLE OF CONTENTS

LIST OF TABLES

Chapter 2

Chapter 3

LIST OF FIGURES

CHAPTER 2

CHAPTER 3

CHAPTER 1: LITERATURE REVIEW

Wheat Production

Wheat (*Triticum aestivum* L.) has been a vital crop since domestication, 10,000 years ago during the Neolithic Revolution, in the Middle East between the Tigris and Euphrates river. This was a crucial transitional period for humankind as hunting and gathering slowly diminished and agriculture-based economies developed (Abbo et al., 2005)**.** It was one of the earliest domesticated crops due to its adaptability, high yield potential, and viscoelastic properties that are the basis of dough used for bread and other food products (Shewry, 2009). Presently, wheat is the third most valuable crop globally, behind maize (*Zea mays)* and rice (*Oryza sativa*) and was grown on approximately 219.7 million hectares globally in 2017, producing 758.3 million metric tons of grain (USDA, 2018). In 2017, 18.58 million hectares of wheat were planted in the US, yielding 37.8 million metric tons; a decrease from 50.2 million metric tons the previous season (Bond and Liefert, 2018).

Classifications of Wheat

Wheat is classified into six market classes based on color, hardness and growing season including: durum, hard white winter (HWW), soft white winter (SWW), soft red winter (SRW), hard red spring (HRS), and hard red winter (HRW) (Bond and Liefert, 2018). The six classes are grown in various regions of the US and for different end-use products. 60% of durum wheat is produced in North Dakota and the remaining 40% in Arizona and California ("U.S. Wheat Associates," 2018). Due to its high protein and gluten content, durum is milled almost entirely for pasta production (Liu et al., 1996)**.** Hard White Winter is primarily grown in North Dakota and Kansas and is used for Asian-style noodles, whole wheat flour and tortilla production ("U.S.

Wheat Associates," 2018). Soft white winter is grown primarily in the Pacific Northwest region of the US (Washington, Oregon, and Idaho). It contains low protein, and weak gluten strength making it ideal to produce cakes and pastries (Kaldy and Rubenthaler, 1987). Hard red spring is grown in the Dakotas and Minnesota and is used to produce designer foods like rolls, croissants, bagels, and pizza and is primarily grown in ("U.S. Wheat Associates," 2018). Hard red winter is the most widely grown and versatile wheat class, milled to produce Asian style noodles, rolls, flat breads, tortillas and all-purpose flour ("U.S. Wheat Associates," 2018). The production area for HRW ranges over several states including the Great Plains of Kansas, Nebraska, Oklahoma and Texas (Bond and Liefert, 2018). Soft red winter accounts for 15 to 20% of US wheat production and is grown primarily in states near the Mississippi River Delta in the Eastern area of the country, including Arkansas. Soft red winter is milled primarily for cakes, cookies, and crackers (Bond and Liefert, 2018).

Arkansas is one of the top-ten producers of SRW wheat in the US, where it is grown in the Mississippi Delta, Arkansas River Valley and the Red River Valley regions of the state. In Arkansas, wheat is planted in the Fall (ideally October 1st -November 20th), following summer annual crops, and harvested the following June (Kelley, 2016). Arkansas farmers often use SRW wheat in rotation with summer annuals, as cover crop, or for animal grazing. In the 2017, SRW wheat was planted on 72,800 hectares in Arkansas; a 49% decrease in comparison to 2016 (NASS, 2017).

Common Wheat Diseases

Fungal pathogens are one of many challenges in wheat production. Considering farming practices, climate, and other factors, many diseases have become more prevalent over time (Chen et al., 2002). Economically important diseases in Arkansas include stripe rust (*Puccinia*

striiformis f. sp. tritici), septoria leaf blotch (*Septoria tritici),* powdery mildew *(Blumaria graminis f. sp tritici)* and *Fusarium* head blight *(Fusarium graminearum)*(Spurlock et al., 2014). Among these, stripe rust has the largest economic impact annually (Spurlock et al., 2014). Stripe rust is caused by the fungal pathogen, *P. striiformis f. sp. tritici,* a macrocyclic pathogen that requires a primary (wheat) and alternate (other grasses) host to complete its life cycle. This fungal pathogen is classified in the phylum Basidiomycota, Class Urediniomycetes, order Uredinales, family Pucciniaceae, genus *Puccinia.* Its species name is specified by the host that it infects.

Stripe Rust

Stripe Rust is a foliar disease of wheat caused by the fungal pathogen *Puccinia striiformis f. sp. tritici*. and is one of the most devastating foliar diseases globally, being reported in more than 60 countries (Stubbs, 1985; Chen, 2005; Chen et al., 2010). It was initially recognized in the United States in Washington in 1915 (Carleton, 1915). The life cycle of stripe rust begins with the dissemination of urediospores by wind or rain onto the leaf surface. Urediospores are asexual and maintain dominance in the population on the primary host. The ability of urediospores to be transported by wind in the asexual stage results in large-scale epidemics in cereal crops (Chen et al., 2002). Infection by stripe rust can occur at any time during the wheat life cycle, from the seedling stage, to plant maturity (Chen, 2005). Under optimum conditions, spore germination begins within three hours from initial infection.

All three rust pathogens (stripe rust, leaf rust and stem rust) are obligate parasites with different optimum temperature ranges for disease development. Stripe rust is a moist-environment and cool-temperature disease with optimum growing temperatures from 7-12 °C (Line and Chen, 1995). Stripe rust is highly active during the night due to dew formation and

lower temperatures (Stubbs, 1985). Stripe rust has also developed adaptation to higher temperatures, with a maximum germination temperature reaching 20 °C and a latent period of 8.5 days. (Schroeder, 1964; Milus et al., 2006). Symptoms are easily identified within one week after initial infection with or without sporulation (Chen, 2005). Five to seven days following infection, sporulation begins and a cluster of yellow-orange pustules, called uredia can be found on leaf sheaths, necks and glumes. After penetrating and infecting the vein of the leaf, the arrangement of the pustules on the plant resembles a stripe (Emge and Shrum, 1976).

The disease develops in "hot spots" throughout a field that can grow up to 10 m in diameter. Once temperatures reach 25 °C or greater, the production of urediospores is reduced or ceases completely and black teliospores are produced in preparation for overwintering stages. Temperatures below -10 °C can halt or terminate the pathogen (Chen, 2005). However, if winter temperatures are mild, teliospores can germinate to form haploid basidiospores, enabling survival on an alternate host like the Oregon Grape (*Mahonia aquifolium*) (Wang and Chen, 2013).

In the southern areas of the US, stripe rust survives throughout mild winter months and remains in the uredia form if its host has not become senescent, which continues the dissemination of uredia (Line and Chen, 1995). Contingent on the growth stage when infection occurs, stripe rust can drastically reduce kernels per spike, test weight and grain yield. Though stripe rust is not a seed-borne disease, like *Fusarium* head blight, its ability to decimate wheat grain yield and quality up to 70% is just as concerning on a global level (Line and Chen, 1995).

Resistance to Stripe Rust

While an integrated management approach including genetic resistance, fungicide application and proper cultural practices is necessary for control, genetic resistance is the most efficient and effective strategy to minimize crop losses (Chen, 2005; Ellis et al., 2014; Singh et al., 2016).

More than 70 stripe rust resistance genes have been identified to date (Yang et al., 2016; McIntosh et al., 2017) . These genes are classified into two major gene types, all-stage resistance (ASR)/seedling resistance and adult plant resistance (APR).

All-stage resistance genes are effective throughout the wheat life cycle, barring a race change. ASR genes often encode protein receptors that interact with corresponding avirulence effector genes from the pathogen. As a result, these race-specific genes tend to lose effectiveness within a few years of deployment due to resistance genes being overcome by new races of stripe rust (Chen et al., 2009; Singh et al., 2011; Liu et al., 2014). These virulent races have adapted to warmer climates, developed mutations against native ASR genes, have shorter latent periods, and increased spore germination up to 18° C, increasing their dissemination rate and expanding geographically (Chen et al., 2002; Milus et al., 2006; Singh et al., 2016).

Adult Plant Resistance is effective at the post seedling stage, likely at the booting stage (Feekes GS 9 to10). It is controlled by smaller effect quantitative trait loci (QTL), which individually confer only low to moderate levels of resistance, often after there is partial disease development this referred to as “slow rusting” (Wu et al., 2016). Some APR genes may be induced in response to growth temperature and light conditions, referred to as Heat-APR (Wu et al., 2016). Lines possessing APR genes are usually selected in field trials during the growth stages of stem elongation (Feekes 5) to as late as mid-grain fill (Feekes 11.1). Adult plant

resistance is considered more durable than ASR because of epistatic effects; however, this is not to say that some APR genes are not race specific (Hickey et al., 2012). Observations for race specific resistance genes have been reported for different sources of stripe rust APR genes in US SRW wheat and European wheat (Hao et al., 2011; Sørensen et al., 2014). Given that APR may have low or delayed expression, resistance could be expressed too late to protect yield loss, leading to a misinterpretation of its effectiveness (Wu et al., 2016). Most APR genes that are used in crops are most likely due to the combination of non-race specific and race specific genes (Ellis et al., 2014). Some APR genes provide resistance to all three species of rust pathogens, and recent studies show that "near immunity" can be achieved when multiple APR genes are pyramided. (Singh et al., 2014).

Unmanned Aerial Systems

Unmanned Aerial Systems (UAS), also referred to as unmanned aerial vehicles (UAV), remote piloted aircrafts (RPA), or drones, are becoming important tools for the agriculturale industry (Watts et al., 2012). The development and application of UAS parallels that of manned aircrafts, both being pushed by military applications and migrating into civilian usage. The initial use of UASs was based on alleviating dangerous tasks for manned flight stemming from fatal flight accidents during military training. UASs were not used directly in battle but in 1933, Reginald Denny developed them for Army gunners and Naval simulations as aerial targets (Keane and Carr, 2013). The evolution of UASs is still driven primarily by advances in military technology. However, many applications have been discovered for civilian usage for remote sensing, reconnaissance, and scientific data collection (Watts et al., 2012). In the 1990s the National Aeronautics and Space Administration, developed the Environmental Research Aircraft and

Sensory Technology program, which initiated the first major steps into developing protocols in support of UAS in scientific research (Watts et al., 2012).

Types of UAS Platforms

Fixed-wing platforms consist of a rigid wing capable of flight due to the uplift generated by the aircraft's forward airspeed and shape of the wing. They are powered by a combustible engine or electric motor. Like conventional manned aircrafts, fixed-wings are built with ailerons (roll/longitudinal axis), elevators (pitch/lateral axis) and rudders (yaw/vertical axis), for in-flight control (Heaphy et al., 2017). These platforms vary in size, flight endurance, and other capabilities. The largest fixed wing is the U.S. RQ-4 Global Hawk, which is capable of 30 hours of flight time and covering 8200 nautical miles (Cook, 2007). On the other end of the spectrum, smaller fixed-wings like the Parrot Disco, weighing 690 grams, are often used for aerial surveying and crop analysis on a large scale. Advantages of fixed wings are extended flight times, low maintenance, and ability to survey large areas. However, fixed wings often need a runway or launch and recovery system to assist in takeoff and landings and lack the ability to hover or analyze parameters at low altitudes (Marshall et al., 2016).

Vertical take-off and landing (VTOL) platforms ascend by air flowing over a wing. These wings or blades create air movement around a single mast, called a rotor. These platforms have one to eight single rotors attached to one aircraft. The major advantage of the rotor-wing aircraft over the fixed-wing is the ability to take off and land vertically and as such requires minimal space. Forward speed is not necessary to maintain lift, which allows it to hover and assess small-scale agriculture research plots (Heaphy et al., 2017). Other advantages of multi-rotor aircrafts include the compensation for wind during flight and the ability to carry an array of different payloads simultaneously to gather multiple types of data. The biggest drawback of most

multi-rotor aircrafts is attributed to their battery powered motors equating to shorter flight times and are typically unable to cover as much land area as a fixed-wing aircraft (Heaphy et al., 2017).

VTOL aircrafts range in size as well. For example, the Kaman K-MAX is the largest unmanned helicopter, weighing 2,721 kg and is used primarily to deliver supplies to military ground units in high threat environments (Mansur et al., 2011). On the other end of the spectrum, the DJI Mavic series (SZ DJI Technology Co., Ltd., Shenzhen, GD, CHN) includes the Mavic Pro, Mavic 2, Mavic Air, and Mavic Mini, ranging from 249g to 743g. The Mavic series aircrafts are used for recreation, professional photography and video, surveillance, land assessments, etc.

High Throughput Phenotyping

The art and science of phenotyping is a key component for genetic improvement of domesticated plants (Fehr, 1991; Haghighattalab et al., 2016). However, phenotyping large breeding nurseries requires substantial investment in time, cost, and labor (Haghighattalab et al., 2016). High throughput phenotyping (HTP) platforms have emerged as a method to obtain detailed measurements of phenotypic traits (Finkel, 2009). The objective of HTP is to characterize large numbers of genotypes using a fraction of the time and labor of manual phenotyping methods (Poland and Price, 2015). Initially, HTP was primarily used in robotic greenhouse operations, where the most commonly used application was assessing shoot biomass by acquiring digital images of plants at specified orientations with known illumination conditions; however, these operations were limited in their two-dimensional analysis and scale in comparison to field experiments (Fanourakis et al., 2014). The two dimensional images alluded to overlapping leaves and stems and led to the underestimation of plant size and other characteristics (Fanourakis et al., 2014; Poland and Price, 2015). Field conditions on the other hand are heterogeneous, but

simulate conditions the genotypes will grow in (Araus and Cairns, 2014). Field-based HTP systems are one of few approaches that offer the accuracy of trait measurements in a large population with repeated measurements, while being cost effective and less tedious. (Poland and Price, 2015).

Remote sensing has been a catalyst in field based HTP of large breeding populations. Phenotyping using remote sensing is the process of measuring a population of lines from a distance using a non-destructive and non-invasive approaches (Araus and Cairns, 2014; Marshall et al., 2016). Remote sensing measurements are derived from electromagnetic radiation. When the radiation reaches a surface, the reflection of the energy is dependent upon the smoothness and uniformity of the surface. If not uniform the energy can be reflected in many directions, diffusing the reflectance. However, some radiation can be absorbed, depending upon the thickness of the object, and the amount of radiation exposure (Curtis, 1991). Through the photosynthetic pigments of plants, healthy plants absorb specific wavelengths of visible light and reflect other wavelengths on the electromagnetic spectrum. Chlorophyll A is the most abundant pigment in plants. It absorbs blue wavelengths (~430nm) and red wavelengths (~662nm) (Knipling, 1970). Leaf reflectance is low throughout the electromagnetic spectrum, until it peaks at the green wavelengths (~550nm) and increases, when it reaches the infrared range (~700-1300nm) (Knipling, 1970). Crop health assessments are determined by this photosynthetic activity when captured by different types of sensors.

Visible spectrum/near infrared (VIS/NIR), long wave infrared sensors , and conventional digital cameras are commonly utilized in field-based HTP; however, improved variations and combinations of these sensors are developed daily (Araus and Cairns, 2014).

Visible/Near-Infrared (VIS/NIR) sensors capture wavelengths between 400-660nm (VIS) and 700-1100nm (NIR) on the electromagnetic spectrum. Visible sensors generally capture three red (665nm), green (550nm), and blue (425) wavelengths. Near-infrared sensors behave in an identical manner, but are modified to capture NIR wavelengths (Marshall et al., 2016). Multispectral and hyperspectral sensors are popular as they measure reflected energy over several bands.

Hyperspectral sensors capture reflected energy in narrow and numerous bands, upwards of 100 bands per pixel. With such immense amount of data, this sensor detects subtle variations in reflected energy, and allows the assessment of complex traits, such as canopy fluorescence and photosynthesis under natural sunlight (Zarco-Tejada et al., 2013). This sensor is larger than most sensors and is sensitive to vibration, requiring a larger aircraft to support its weight and maintain stability during flight.

Multispectral sensors capture reflected energy in 3 to 10 bands, typically visible green, visible red, visible blue, NIR, etc. and are portable compared to hyperspectral sensors. Multispectral imagery has been used in several agricultural applications like mapping wetland vegetation (Adam et al., 2010), estimating leaf area index (Asrar et al., 1985), determining plant height (Fanourakis et al., 2014), crop yield predictions (Yu et al., 2016), phenotyping for large breeding populations (Haghighattalab et al., 2016) quantifying turf grass (Karcher and Richardson, 2003), classifying plant diseases (Kumar et al., 2016) and more.

Long wave infrared sensors gather data beyond 1800 nanometers on the electromagnetic spectrum (Marshall et al., 2016). The images are a wide spectrum of monochromatic images, representing thermal emission in response to the intensity of heat. Long-wave infrared sensors

have been used to monitor drought tolerance, and to detect biotic and abiotic stresses in crops. (Jones, 2006; Berger et al., 2010; Munns et al., 2010).

The early application of field-based high-throughput phenotyping involved the usage of high clearance tractors and other 'phenomobiles' equipped with global positioning system (GPS) or global navigation satellite system (GNSS) technology along with active and passive sensors that monitored photosynthetic activity (Bausch and Delgado, 2005; Montes et al., 2011; Comar et al., 2012). For example, a cart was used to position ultrasonic proximity sensors to measure morphological characteristics of bushy plants in 1989 (Ruixiu et al., 1989). Andrade-Sanchez et al (2014) used a tractor mounted with remote sensors to measure canopy height, reflectance, and temperature simultaneously in cotton at the rate of 0.84 ha hr^{-1}. While this approach was accurate and decreased laborious techniques, time expenditure and portability remained limitations.

Unlike phenomobiles, UASs allow the analysis of entire populations simultaneously, and have become increasingly popular in precision agricultural techniques and high-throughput phenotyping. For UASs to be effective, data processing software is required for platform control, data gathering, and data extraction. Autonomous flight software allows the creation of mission plans including logistics (elevation, image overlap/side-lap, flight path, drone speed, flight time), determining the area of interest, and survey type, making data acquisition easy and repetitive. This reduces error and increases image accuracy in comparison to full-control flights (Marshall et al., 2016). UAS photogrammetry is very accurate, much like real time kinematic (RTK) GPS data, making it possible for UAS photogrammetry to be used in land surveying and crop scouting (Uysal et al., 2015).

Vegetative Indices

Vegetative indices were developed to observe two or more spectral wavelengths, according to mathematic formulas to derive single spectrally-based numbers (Wanjura and Hatfield, 1987). The indices respond to the amount of photosynthetically active tissue within a plant (Wiegand et al., 1986). Some vegetative indices offer a general form of information regarding multiple crops, while other indices detect specific phenotypic characteristics from one index to the next. This leads to the increase in development of vegetative indices and research analyzing their efficacy to detect vegetative symptoms due to nutrient deficiencies, biotic, and abiotic stresses(Wiegand et al., 1986; Devadas et al., 2009, 2015).

Normalized Difference Vegetative Index (NDVI) is widely used across many agricultural and environmental disciplines. It is defined as the differenced ratio of reflectance in the red and near infrared wavelength; initially prompted by the motivation to assess winter wheat dry matter using Landsat satellite data (Tucker, 1979). However, with the use of proximal and remote sensing, field and plot level research has discovered various uses of NDVI in the evaluation of other agronomic traits including: indirect selection for waterlogging tolerance in wheat (Arguello et al., 2016), heat and drought stress tolerance (Reynolds et al., 2007), estimating nitrogen uptake and efficiency (Heege et al., 2008; Magney et al., 2016), estimating grain yield (Aparicio et al., 2000), rating spot blotch disease (Kumar et al., 2016), and has shown promise for high-throughput phenotyping in breeding programs (Haghighattalab et al., 2016; Duan et al., 2017). NDVI values range from -1.0 to 1.0 are linearly correlated with leaf area index (LAI) and biomass production (Kross et al., 2015). This index is broadly suited for stress detection among crops and can distinguish between yellow rust from healthy leaves in wheat (Devadas et al., 2009; Su et al., 2018).

The dark green color index was developed to measure dark green color of biomass in digital imaging, after discovering that amounts of red and blue alters the green color in images (Karcher and Richardson, 2003). This index is significant in the ability to quantify turf grass color and has also found a strong relationship between yield, leaf nitrogen and corn greenness (Rorie et al., 2011). It functions by using the average of a transformed hue, saturation and brightness (HSB) values. HSB values are based on human perception of color, where hue is defined as the angle on a continuous circular scale from 0° to 360° (0°=red, 60°=yellow, 120°=green, 180°=cyan, 240°=blue, 300°=magenta) saturation is the purity of the color from 0% (gray) to 100% (fully saturated) and brightness is relative lightness or darkness of the color from 0% (black) to 100% white) (Purcell et al., 2013). The dark green hue transform is calculated as *Hue – 60/60,* so that hues of 60 and 120 would equal to dark green hue transforms of zero and one. Since lower saturation and brightness values correspond to darker green colors, *1 – saturation* and *1 – brightness* was used to calculate the dark green color transforms for saturation and brightness. After taking the average of transformed HSB values, a single measure of dark green color ranging from zero to one are yielded, with higher values corresponding to dark green color (Karcher and Richardson, 2003).

Genome-Wide Association Studies

Genome-Wide Association Studies (GWAS) are experimental designs that detect associations between genetic variants and traits of interest within a given population and have been used to understand the genetic sources behind phenotypic variation in humans, plants and animals, being more successful in plants than the others (Brachi et al., 2011; Visscher et al., 2017). In globally produced food crops like maize, rice, and wheat, GWASs have been used to identify quantitative trait loci (QTL) associated with, disease resistance (Kertho et al., 2015;

Kumar et al., 2015), stress tolerance (Farfan et al., 2015), nutrition quality, yield,(Huang et al., 2010) and more.

Although linkage mapping remains significant, it suffers at only being capable of identifying traits in specific regions of a genome in either F2 populations or recombinant inbred lines, and it lacks mapping resolution due to the amount of recombination that occurs within recombinant inbred lines. However, GWASs overcome this limitation by using historic recombination events and using larger panels of diverse, unrelated individuals. With the increased variation, recombination events increase, thus increasing the mapping resolution (Brachi et al., 2011; Korte and Farlow, 2013).

Many research projects have used GWASs in efforts of identifying stripe rust resistance QTL. One previous study evaluated 567 winter wheat lines provided by NSGC representing 44 countries against five races of stripe rust previously identified in North Dakota. The association analysis identified 31 QTL markers associated with resistance to all five races of stripe rust (Kertho et al., 2015).

References

Abbo, S., A. Gopher, B. Rubin, and S. Lev-Yadun. 2005. On the Origin of Near Eastern Founder Crops and the 'Dump-heap Hypothesis.' Genet Resour Crop Evol 52(5): 491–495. doi: 10.1007/s10722-004-7069-x.

Adam, E., O. Mutanga, and D. Rugege. 2010. Multispectral and hyperspectral remote sensing for identification and mapping of wetland vegetation: a review. Wetlands Ecology and Management; Dordrecht 18(3): 281–296. doi: http://dx.doi.org/10.1007/s11273-009-9169-z.

Andrade-Sanchez, P., M.A. Gore, J.T. Heun, K.R. Thorp, A.E. Carmo-Silva, et al. 2014. Development and evaluation of a field-based high-throughput phenotyping platform. Functional Plant Biol. 41(1): 68–79. doi: 10.1071/FP13126.

Araus, J.L., and J.E. Cairns. 2014. Field high-throughput phenotyping: the new crop breeding frontier. Trends in Plant Science 19(1): 52–61. doi: 10.1016/j.tplants.2013.09.008.

Asrar, G., E.T. Kanemasu, and M. Yoshida. 1985. Estimates of leaf area index from spectral reflectance of wheat under different cultural practices and solar angle. Remote Sensing of Environment 17(1): 1–11. doi: 10.1016/0034-4257(85)90108-7.

Bausch, W.C., and J.A. Delgado. 2005. Impact of Residual Soil Nitrate on In-Season Nitrogen Applications to Irrigated Corn Based on Remotely Sensed Assessments of Crop Nitrogen Status. Precision Agriculture; Dordrecht 6(6): 509–519. doi: http://0-dx.doi.org.library.uark.edu/10.1007/s11119-005-5641-9.

Berger, B., B. Parent, and M. Tester. 2010. High-throughput shoot imaging to study drought responses. J Exp Bot 61(13): 3519–3528. doi: 10.1093/jxb/erq201.

Bond, J.K., and O. Liefert. 2018. USDA ERS Wheat Outlook: August 2018. https://www.ers.usda.gov/publications/pub-details/?pubid=89837 (accessed 14 October 2018).

Brachi, B., G.P. Morris, and J.O. Borevitz. 2011. Genome-wide association studies in plants: the missing heritability is in the field. Genome Biology 12(10): 232. doi: 10.1186/gb-2011-12-10-232.

Carleton, M.A. 1915. Hard wheats winning their way. US Department of Agriculture.

Chen, X.M. 2005. Epidemiology and control of stripe rust [*Puccinia striiformis* f. sp. *tritici*] on wheat. Canadian Journal of Plant Pathology 27(3): 314–337. doi: 10.1080/07060660509507230.

Chen, X., M. Moore, E.A. Milus, D.L. Long, R.F. Line, et al. 2002. Wheat Stripe Rust Epidemics and Races of Puccinia striiformis f. sp. tritici in the United States in 2000. Plant Disease 86(1): 39–46. doi: 10.1094/PDIS.2002.86.1.39.

Chen, X., L. Penman, A. Wan, and P. Cheng. 2010. Virulence races of Puccinia striiformis f. sp. tritici in 2006 and 2007 and development of wheat stripe rust and distributions, dynamics, and evolutionary relationships of races from 2000 to 2007 in the United States. Canadian Journal of Plant Pathology 32(3): 315–333. doi: 10.1080/07060661.2010.499271.

Chen, W.Q., L.R. Wu, T.G. Liu, S.C. Xu, S.L. Jin, et al. 2009. Race Dynamics, Diversity, and Virulence Evolution in Puccinia striiformis f. sp. tritici, the Causal Agent of Wheat Stripe Rust in China from 2003 to 2007. Plant Disease 93(11): 1093–1101. doi: 10.1094/PDIS-93-11-1093.

Comar, A., P. Burger, B. de Solan, F. Baret, F. Daumard, et al. 2012. A semi-automatic system for high throughput phenotyping wheat cultivars in-field conditions: description and first results. Functional Plant Biol. 39(11): 914–924. doi: 10.1071/FP12065.

Cook, K.L.B. 2007. The Silent Force Multiplier: The History and Role of UAVs in Warfare. 2007 IEEE Aerospace Conference. p. 1–7

Curtis, L.F. 1991. Remote sensing principles, sensors, platfroms, and data. Remote Sensing for Hazard Monitoring and Disaster Assessment: Marine and Coastal Applications in the Mediterranean Region 2: 19.

Devadas, R., D.W. Lamb, D. Backhouse, and S. Simpfendorfer. 2015. Sequential application of hyperspectral indices for delineation of stripe rust infection and nitrogen deficiency in wheat. Precision Agriculture; Dordrecht 16(5): 477–491. doi: http://0-dx.doi.org.library.uark.edu/10.1007/s11119-015-9390-0.

Devadas, R., D.W. Lamb, S. Simpfendorfer, and D. Backhouse. 2009. Evaluating ten spectral vegetation indices for identifying rust infection in individual wheat leaves. Precision Agriculture; Dordrecht 10(6): 459–470. doi: http://0-dx.doi.org.library.uark.edu/10.1007/s11119-008-9100-2.

Ellis, J.G., E.S. Lagudah, W. Spielmeyer, and P.N. Dodds. 2014. The past, present and future of breeding rust resistant wheat. Front. Plant Sci. 5. doi: 10.3389/fpls.2014.00641.

Emge, R.G., and R.D. Shrum. 1976. Epiphytology of Puccinia striiformis at five selected locations in Oregon during 1968 and 1969. Phytopathology 66: 1406–1412.

Fanourakis, D., C. Briese, J.F. Max, S. Kleinen, A. Putz, et al. 2014. Rapid determination of leaf area and plant height by using light curtain arrays in four species with contrasting shoot architecture. Plant Methods 10(1): 9. doi: 10.1186/1746-4811-10-9.

Fehr, W. 1991. Principles of cultivar development: theory and technique. Macmillian Publishing Company.

Finkel, E. 2009. With ‘phenomics,’plant scientists hope to shift breeding into overdrive. American Association for the Advancement of Science.

Haghighattalab, A., L.G. Perez, S. Mondal, D. Singh, D. Schinstock, et al. 2016. Application of unmanned aerial systems for high throughput phenotyping of large wheat breeding nurseries. Plant Methods; London 12. doi: http://0-dx.doi.org.library.uark.edu/10.1186/s13007-016-0134-6.

Hao, Y., Z. Chen, Y. Wang, D. Bland, J. Buck, et al. 2011. Characterization of a major QTL for adult plant resistance to stripe rust in US soft red winter wheat | SpringerLink. https://link.springer.com/article/10.1007/s00122-011-1675-8 (accessed 6 March 2019).

Heaphy, M., M.S. Watt, J.P. Dash, and G.D. Pearse. 2017. UAVs for data collection-plugging the gap. New Zealand Journal of Forestry 62(1): 23–30.

Hickey, L.T., P.M. Wilkinson, C.R. Knight, I.D. Godwin, O.Y. Kravchuk, et al. 2012. Rapid phenotyping for adult-plant resistance to stripe rust in wheat. Plant Breeding 131(1): 54–61. doi: 10.1111/j.1439-0523.2011.01925. x.

Jones, H.G. 2006. Monitoring plant and soil water status: established and novel methods revisited and their relevance to studies of drought tolerance. Journal of experimental botany 58(2): 119–130.

Kaldy, M.S., and G.L. Rubenthaler. 1987. Milling, baking and physical-chemical properties of selected soft white winter and spring wheats. Cereal Chem 64(5): 302–307.

Karcher, D.E., and M.D. Richardson. 2003. Quantifying turfgrass color using digital image analysis. Crop Science 43(3): 943–951. doi: 10.2135/cropsci2003.9430.

Keane, J.F., and S.S. Carr. 2013. A brief history of early unmanned aircraft. Johns Hopkins APL Technical Digest 32(3): 558–571.

Kelley, J. 2016. Making Wheat Profitable in 2016. https://www.uaex.edu/farm-ranch/crops-commercial-horticulture/wheat/.

Kertho, A., S. Mamidi, J.M. Bonman, P.E. McClean, and M. Acevedo. 2015. Genome-Wide Association Mapping for Resistance to Leaf and Stripe Rust in Winter-Habit Hexaploid Wheat Landraces. PLoS One; San Francisco 10(6): e0129580. doi: http://0-dx.doi.org.library.uark.edu/10.1371/journal.pone.0129580.

Knipling, E.B. 1970. Physical and physiological basis for the reflectance of visible and near-infrared radiation from vegetation. Remote sensing of environment 1(3): 155–159.

Korte, A., and A. Farlow. 2013. The advantages and limitations of trait analysis with GWAS: a review. Plant Methods 9(1): 29. doi: 10.1186/1746-4811-9-29.

Kross, A., H. McNairn, D. Lapen, M. Sunohara, and C. Champagne. 2015. Assessment of RapidEye vegetation indices for estimation of leaf area index and biomass in corn and soybean crops. International Journal of Applied Earth Observation and Geoinformation 34: 235–248.

Kumar, S., M.S. Röder, R.P. Singh, S. Kumar, R. Chand, et al. 2016. Mapping of spot blotch disease resistance using NDVI as a substitute to visual observation in wheat (Triticum aestivum L.). Molecular Breeding; Dordrecht 36(7): 1–11. doi: http://0-dx.doi.org.library.uark.edu/10.1007/s11032-016-0515-6.

Line, R.F., and X. Chen. 1995. Successes in breeding for and managing durable resistance to wheat rusts. Plant Disease 79(12): 1254–1255.

Liu, W., M. Frick, R. Huel, C.L. Nykiforuk, X. Wang, et al. 2014. The stripe rust resistance gene Yr10 encodes an evolutionary-conserved and unique CC–NBS–LRR sequence in wheat. Molecular plant 7(12): 1740–1755.

Liu, C.Y., K.W. Shepherd, and A.J. Rathjen. 1996. Improvement of durum wheat pastamaking and breadmaking qualities. Cereal Chem 73(2): 155–166.

Mansur, M.H., M.B. Tischler, M.D. Bielefield, J.W. Bacon, K.K. Cheung, et al. 2011. Full Flight Envelope Inner Loop Control Law Development for the Unmanned K-MAX. ARMY AVIATION AND MISSILE RESEARCH DEVELOPMENT AND ENG CTR MOFFETT FIELD CA MOFFETT FIELD United States.

Marshall, D.M., R.K. Barnhart, S.B. Hottman, E. Shappee, and M.T. Most. 2016. Introduction to unmanned aircraft systems. Crc Press.

McIntosh, R.A., J. Dubcovsky, J.W. Rogers, C.F. Morris, R. Appels, et al. 2017. Catalogue of gene symbols for wheat: 2017 supplement. https://shigen.nig.ac.jp/wheat/komugi/genes/macgene/supplement2017.pdf.

Milus, E.A., E. Seyran, and R. McNew. 2006. Aggressiveness of Puccinia striiformis f. sp. tritici Isolates in the South-Central United States. Plant Disease 90(7): 847–852. doi: 10.1094/PD-90-0847.

Montes, J.M., F. Technow, B.S. Dhillon, F. Mauch, and A.E. Melchinger. 2011. High-throughput non-destructive biomass determination during early plant development in maize under field conditions. Field Crops Research 121(2): 268–273. doi: 10.1016/j.fcr.2010.12.017.

Munns, R., R.A. James, X.R.R. Sirault, R.T. Furbank, and H.G. Jones. 2010. New phenotyping methods for screening wheat and barley for beneficial responses to water deficit. J Exp Bot 61(13): 3499–3507. doi: 10.1093/jxb/erq199.

NASS, U. 2017. Census of Agriculture: Arkansas State and County Data, 2002. USDA National Agricultural Statistics Service.

Poland, J., and K. Price. 2015. Plant high-throughput phenotyping using photogrammetry and 3D modeling techniques.

Purcell, L.C., R.L. Rorie, and D.E. Karcher. 2013. System and method of determining nitrogen levels from a digital image.

Rorie, R.L., L.C. Purcell, D.E. Karcher, and C.A. King. 2011. The Assessment of leaf nitrogen in corn from digital images. Crop Science 51(5): 2174–2180. doi: 10.2135/cropsci2010.12.0699.

Ruixiu, S., J.B. Wilkerson, L.R. Wilhelm, and F.D. Tompkins. 1989. A microcomputer-based morphometer for bush-type plants. Computers and Electronics in Agriculture 4(1): 43–58. doi: 10.1016/0168-1699(89)90013-6.

Schroeder, J. 1964. Investigations on germination of uredospores of stripe rust (puccinia striiformis west). army biological labs Fredrick, MD. ARMY BIOLOGICAL LABS FREDERICK MD.

Shewry, P.R. 2009. Wheat. J Exp Bot 60(6): 1537–1553. doi: 10.1093/jxb/erp058.

Singh, R.P., S. Herrera-Foessel, J. Huerta-Espino, S. Singh, S. Bhavani, et al. 2014. Progress towards genetics and breeding for minor genes-based resistance to Ug99 and other rusts in CIMMYT high-yielding spring wheat. Journal of Integrative Agriculture 13(2): 255–261. doi: 10.1016/S2095-3119(13)60649-8.

Singh, R.P., J. Huerta-Espino, S. Bhavani, S.A. Herrera-Foessel, D. Singh, et al. 2011. Race non-specific resistance to rust diseases in CIMMYT spring wheats. Euphytica 179(1): 175–186. doi: 10.1007/s10681-010-0322-9.

Singh, R.P., P.K. Singh, J. Rutkoski, D.P. Hodson, X. He, et al. 2016. Disease impact on wheat yield potential and prospects of genetic control. Annual Review of Phytopathology 54(1): 303–322. doi: 10.1146/annurev-phyto-080615-095835.

Sørensen, C.K., M.S. Hovmøller, M. Leconte, F. Dedryver, and C. de Vallavieille-Pope. 2014. New races of puccinia striiformis found in europe reveal race specificity of long-term effective adult plant resistance in wheat. Phytopathology 104(10): 1042–1051. doi: 10.1094/PHYTO-12-13-0337-R.

Spurlock, T., T. Faske, T. Kirkpatrick, G. Milus, and J. Kelley. 2014. Important wheat diseases in Arkansas and their management.: 14.

Stubbs, R.W. 1985. 3 - Stripe Rust. In: Roelfs, A.P. and Bushnell, W.R., editors, Diseases, Distribution, Epidemiology, and Control. Academic Press. p. 61–101

Su, J., C. Liu, M. Coombes, X. Hu, C. Wang, et al. 2018. Wheat yellow rust monitoring by learning from multispectral UAV aerial imagery. Computers and Electronics in Agriculture 155: 157–166. doi: 10.1016/j.compag.2018.10.017.

Tucker, C.J. 1979. Red and photographic infrared linear combinations for monitoring vegetation. Remote Sensing of Environment 8(2): 127–150. doi: 10.1016/0034-4257(79)90013-0.

U.S. Wheat Associates. 2018. Wheat Classes. https://www.uswheat.org/working-with-buyers/wheat-classes/ (accessed 24 August 2018).

USDA, F. 2018. World Agricultural Production. https://apps.fas.usda.gov/psdonline/circulars/production.pdf (accessed 14 October 2018).

Uysal, M., A.S. Toprak, and N. Polat. 2015. DEM generation with UAV Photogrammetry and accuracy analysis in Sahitler hill. Measurement 73: 539–543. doi: 10.1016/j.measurement.2015.06.010.

Visscher, P.M., N.R. Wray, Q. Zhang, P. Sklar, M.I. McCarthy, et al. 2017. Ten years of GWAS discovery: Biology, function, and translation. The American Journal of Human Genetics 101(1): 5–22. doi: 10.1016/j.ajhg.2017.06.005.

Wang, M.N., and X.M. Chen. 2013. First report of Oregon grape (Mahonia aquifolium) as an alternate host for the wheat stripe rust pathogen (Puccinia striiformis f. sp. tritici) under artificial inoculation. Plant Disease 97(6): 839–839. doi: 10.1094/PDIS-09-12-0864-PDN.

Wanjura, D.F., and J.L. Hatfield. 1987. Sensitivity of spectral vegetative indices to crop biomass. Transactions of the ASAE 30(3): 810–0816.

Watts, A.C., V.G. Ambrosia, E.A. Hinkley, A.C. Watts, V.G. Ambrosia, et al. 2012. Unmanned aircraft systems in remote sensing and scientific research: classification and considerations of use. Remote Sensing 4(6): 1671–1692. doi: 10.3390/rs4061671.

Wiegand, C.L., A.J. Richardson, and P.R. Nixon. 1986. Spectral components analysis: a bridge between spectral observations and agrometeorological crop models. IEEE transactions on geoscience and remote sensing (1): 83–89.

Wu, X.-L., J.-W. Wang, Y.-K. Cheng, X.-L. Ye, W. Li, et al. 2016. Inheritance and Molecular Mapping of an All-Stage Stripe Rust Resistance Gene Derived from the chinese common wheat landrace "Yilongtuomai." Journal of Heredity 107(5): 463–470. doi: 10.1093/jhered/esw032.

Yang, E., G. Li, L. Li, Z. Zhang, W. Yang, et al. 2016. Characterization of stripe rust resistance genes in the wheat cultivar Chuanmai45. Int J Mol Sci 17(4). doi: 10.3390/ijms17040601.

Yu, N., L. Li, N. Schmitz, L.F. Tian, J.A. Greenberg, et al. 2016. Development of methods to improve soybean yield estimation and predict plant maturity with an unmanned aerial vehicle-based platform. Remote Sensing of Environment 187: 91–101. doi: 10.1016/j.rse.2016.10.005.

Zarco-Tejada, P.J., A. Catalina, M.R. González, and P. Martín. 2013. Relationships between net photosynthesis and steady-state chlorophyll fluorescence retrieved from airborne hyperspectral imagery. Remote Sensing of Environment 136: 247–258. doi: 10.1016/j.rse.2013.05.011.

CHAPTER 2: UTILITY OF UAS TO ASSESS STRIPE RUST SEVERITY AND DETECT KNOWN RESISTANCE GENES IN A SOFT RED WINTER WHEAT BREEDING NURSERY

Abstract

Stripe Rust (*Puccinia striiformis* f. sp. *tritici*) is an economically important fungal pathogen of wheat, however, resistant cultivars provide the most efficient method of control. High-throughput phenotyping using unmanned aircraft systems (UAS) offers a potentially more efficient method for field-based phenotyping compared to visual assessment. However, there is limited research in this area and further proof of concept is warranted. In this study, the ability of remote sensing to predict stripe rust severity was evaluated in a diverse population of 594 soft red winter wheat lines, over two years. Genotypes were sown in single-row plots to mimic the progeny-row generation of breeding and were inoculated. Ground measurements were obtained by visually rating stripe rust intensity, and normalized difference vegetation index (NDVI), blue NDVI (BNDVI), and dark green color index (DGCI) were obtained using a UAS. In 2018, significant (p<0.0001) relationships were observed between visual severity and DGCI (R^2 = 0.54) and visual severity and BNDVI (R^2 = 0.12). Similar relationships were observed in 2019 with DGCI (R^2 = 0.16, p<0.0001) and NDVI (R^2 = 0.36, p<0.0001) with visual severity. When combined across years the linear relationship between visual severity and DGCI increased (R^2 = 0.58). A genome-wide association study (GWAS) identified peaks on chromosomes 1B, 2A, and 4B that were consistent between visual ratings and DGCI and were consistent with the location of known stripe rust resistance genes. Additional research is needed to assess the effect of plot size and evaluate other indices that might improve the prediction of stripe rust severity using UAS.

Introduction

Stripe Rust is a foliar disease of wheat caused by the fungal pathogen *Puccinia striiformis f. sp. tritici*. It is one of the most devastating wheat diseases globally, reported in more than 60 countries (Stubbs, 1985; Chen, 2005; Chen et al., 2010). Yield losses from 50% to 100% may occur in susceptible cultivars if infection occurs early in the growing season with cool and wet conditions (Chen et al., 2002; Wegulo and Byamukama, 2012). In the US, stripe rust was first identified in Washington in 1915 with the first notable outbreak during the 1950s occurring in the western part of the state (Carleton, 1915; Chen, 2007). US wheat production lost due to stripe rust exceeded 6.4 million metric tons in 2016 across 30 states (Chen, 2007; USDA, 2016). The spread of stripe rust has resulted from new races of *P. striiformis* that have overcome deployed resistance genes and as such, pose a constant challenge to wheat breeders and producers (Line, 2002; Chen et al., 2010). While an integrated management approach that includes genetic resistance, fungicide applications, and the proper cultural practices is necessary, genetic resistance remains the most cost efficient and effective (Chen, 2005; Singh et al., 2016).

There are two major types of stripe rust resistance. All-stage resistance (ASR) is effective beginning at the seedling stage and barring a race change, continues throughout the entire life cycle (Chen, 2005). ASR genes often encode protein receptors that interact with corresponding avirulence effector genes from the pathogen. As a result, these race-specific genes tend to lose effectiveness within a few years of deployment due to resistance genes being overcome by new races of stripe rust (Singh et al., 2011; Liu et al., 2014). Many *P. striiformis* races, such as *PstS*1 and *PstS*2, are now adapted to warmer temperatures, increasing spore germination at temperatures up to 18° C. These strains have developed mutations against native ASR genes, and

have shorter latent periods at 18° C than at 12° C (Chen et al., 2002; Milus et al., 2006; Singh et al., 2016).

Adult plant resistance (APR) is primarily effective at the post seedling stage and is quantitatively inherited. APR is conferred by smaller effect quantitative trait loci (QTL) that individually provide only low to moderate resistance after initial infection has occurred. This is referred to as "slow rusting" (Wu et al., 2016). Due to its polygenic control, APR is considered the most durable type of resistance and near immunity may be achieved by pyramiding multiple genes (Chen, 2005; Singh et al., 2011; Rahmatov et al., 2017).

For the past decade, the cost of genotyping has decreased significantly, allowing increased discovery of disease resistance QTL and the application of molecular markers in breeding. Marker-assisted selection (MAS) and more recently genomic selection (GS), are being used to select for stripe rust resistance in combination with phenotypic selection (Rutkoski et al., 2014; Singh et al., 2016). While genotyping technology has progressed rapidly, the development and utilization of new phenotyping methods has been more gradual. The lag connecting genetic variants to observed phenotypes results in a bottleneck in the breeding process due to time requirement to evaluate thousands of genotypes in replicate, and across multiple environments (White et al., 2012).

The agricultural unmanned aerial system (UAS) market is predicted to exceed 4 billion dollars by 2022, due largely to the rise of precision agriculture and crop health assessment applications (Jenkins and Vasigh, 2013; Marshall et al., 2016; Reagan, 2017). High-resolution data from remote sensors mounted to UAS can rapidly capture the absorption and reflection properties of plants based on their photosynthetic activity to determine the health of the plants. (Marshall et al., 2016). Chlorophyll A is the most abundant pigment in plants, absorbing both

blue (~430nm) and red wavelengths (~662nm) (Knipling, 1970). Leaf reflectance is low throughout the electromagnetic spectrum, until reaching the green wavelengths (~550nm), and continues an upward trend of reflectance into the infrared range (~700-1300nm) (Knipling, 1970). Many vegetative indices including the dark green color index (DGCI), normalized difference vegetation index (NDVI), and blue NDVI (BNDVI) were developed from observing the ratios of two or more spectral wavelengths as a proxy for the amount of photosynthetically active tissue (Wiegand et al., 1986; Wanjura and Hatfield, 1987).

DGCI was developed to measure the color of plants in digital images after it was discovered that the amount of red and blue light alters green color (Karcher and Richardson, 2003a). This index is used to quantify the intensity of leaf greenness for nitrogen content in corn (Karcher and Richardson, 2003a) and turf (Rorie et al., 2011).

NDVI is the differenced ratio of reflectance in the red and near infrared wavelengths (Tucker, 1979). It has been used in the evaluation of waterlogging (Arguello et al., 2016), heat, and drought stress tolerance (Reynolds et al., 2007; Haghighattalab et al., 2016; Duan et al., 2017), nitrogen uptake and efficiency (Heege et al., 2008), grain yield prediction (Aparicio et al., 2000), and disease detection (Kumar et al., 2016) . Blue NDVI replaces the red band with blue and serves as an alternative when using a low-cost digital camera.

Currently there is limited proof of concept for the use of remote sensing to assess disease severity in wheat, particularly during the early breeding generation when plot size and replication are limited. The objectives of this study were to (1) evaluate the relationship between remote sensing indices and a visual rating of stripe rust severity, (2) compare remote and proximal measurements of NDVI, and (3) determine the ability to detect stripe rust resistance QTL using UAS.

Materials and Methods

Germplasm

The germplasm used in this study consisted of 594 genotypes from the Gulf Atlantic Wheat Nursery (GAWN). Of these genotypes, 102 were developed by the University of Arkansas, 109 from the University of Georgia, 107 from Louisiana State University Ag Center, 103 from North Carolina State University, 59 from Texas A&M University, 41 from the University of Florida, 40 from Virginia Institute of Technology, 19 from Clemson University, and 14 from private industry or the USDA-ARS. These programs represent the germplasm used in the University of Arkansas Wheat Breeding Program and have varying levels of stripe rust resistance. In addition to the GAWN population, a stripe rust resistant check, 'Pat' (Bacon et al., 2004), and a stripe rust susceptible check, 'Croplan Genetics 514W' (CG514W) were included.

Experimental Design

The study was conducted at the Milo J. Shult Agricultural Research and Extension Center in Fayetteville, Arkansas, over two years (2017-2018 and 2018-2019). The GAWN genotypes were drill-seeded in single-row plots, 1.22 m in length, with 0.38 m spacing between rows and 0.60 m alleys between tiers. In year one, the trial was planted in a randomized complete block design with two replications. In year two, genotypes were planted in an un-replicated augmented design with each block containing the resistant and susceptible checks. The blocks were unbalanced with 94 entries in the first and seventh blocks and 84 entries in the remaining five blocks.

Trials were planted on October 26, 2017 and October 23, 2018. In both years, nitrogen fertilizer in the form of urea was applied after the tillering stage (Feekes 3 to 5) in two applications of 67 kg N ha^{-1} and 33 kg N ha^{-1}, respectively. Plots were rainfed and managed with

Axial (Syngenta AG, Basel, CHE) for ryegrass, Harmony Xtra (DuPont Agroscienes, Wilmington, DE, USA) for winter annuals, and Grizzly (Winfield United, Arden Hills, MN, USA) for aphids.

Stripe Rust Inoculation

Inoculum was collected from susceptible wheat seedlings that were grown in a growth chamber, programmed for a 14-hr photoperiod with a 12° C/8 °C day/night cycle, with uncontrolled humidity. The seedlings were inoculated with a mixture of 1.0 g of talcum powder per 0.01 g of previously stored PST-127 and PST-37 races, using an atomizer. After at least two reproductive life cycles of the pathogen, the inoculum was collected and dried in a desiccator for 12 to 48 hours. The dried spores were then stored at -80° C until field inoculation.

To simulate natural wind dispersion, uridiniospores were applied in the field by a Hudson model 18539 back-pack blower (H.D. Hudson Manufacturing Company, Lowell, MI, USA) with an approximate ratio of 1.0 g: 100.0 g uridinospores to talcum powder ratio. The nursery was surrounded by the susceptible check which provided a continuous source of inoculum after infection. Experimental plots were artificially inoculated six times, beginning at stem elongation (Feekes 4 to 5).

Visual Stripe Rust Severity Evaluations

In year one (2017-2018), each experimental plot was rated for stripe rust severity twice, once at the booting stage (Feekes 9, severity at booting) and again at the grain-fill (Feekes 11.0, severity at grain-fill). In year two, each plot was rated for stripe rust severity three times, once at the beginning of the booting stage (Feekes 9, severity at booting), at the heading stage (Feekes 10.0, severity at heading), and again during grain-fill (Feekes GS 11.0, severity at grain-fill). A

modified Cobb scale was used, which rates percentage of leaf area infected from 0 to 100 in increments (0, 2, 7,15, 30, 50, 70, 85, 93, 98, 100), with 0 showing no sign of infection and 100 being the highest level of infection (Fig.1, Peterson et al., 1948). In year two, area under the disease progress curve (AUDPC) was calculated using the repeated ratings (Madden et al., 2007) and the following formula:

$$AUDPC = \sum_{i=1}^{N_i-1} \frac{(y_i+y_{i+1})}{2}(t_{i+1} - t_i)$$

where y_i is an assessment of the disease severity rating at the ith observation, t_i is the time component (in days) of the ith observation, and n is the total number of observations. Values greater than 0 indicated progression of stripe rust over the 14-day time period of the repeated measure.

Platforms and Cameras Used to Capture Remote Sensing Data

In year one, the Phantom 4 Pro (SZ DJI Technology Co., Ltd., Shenzhen, GD, CHN) quadcopter, equipped with an integrated global positioning system (GPS) and global national satellite system (GLONASS) was used to capture red, green, blue (RGB) and near infrared (NIR) images. The payload included a 20-megapixel complementary metal oxide semiconductor (CMOS) sensor and a Canon S110 camera (Canon Inc., Tokyo, JPN). RGB images were captured using the CMOS sensor and NIR images captured using the Canon S110 modified to Blue-Green-NIR (400-760nm). The ground station pro application (SZ DJI Technology Co., Ltd., Shenzhen, GD, CHN) was used for autonomous flight navigation, based on ground coordinates utilizing the spline survey option.

In year two (2018-2019), the DJI Matrice 200 quadcopter, equipped with a downwelling light sensor, global positioning system (GPS) magnetometer module, and a RedEdge M

multispectral sensor, all developed by MicaSense (MicaSense, Inc, Seattle, WA, USA), was used for image capture (SZ DJI Technology Co., Ltd., Shenzhen, GD, CHN). The RedEdge M captures five images (1280 x 800) for five bands, including green, blue, red, red-edge, and near infrared (475-840nm). A combination of the DJI GO 4 application and the sensor Wi-Fi connection was applied to execute autonomous flights and monitor the multispectral sensor during data collection.

Ground NDVI measurements were captured using the Greenseeker Handheld Optical Sensor in year two (Trimble, Inc, Sunnyvale, CA, USA). Readings were gathered by walking between the adjacent plots, with the sensor held over the plots at 0.50 m, near solar noon and in time proximity to the visual ratings (Greenseeeker booting, heading, grain-fill).

Remote Sensing Data Collection

In 2018, UAS data collection were collected on April 19 and May 4 and visual severity ratings on April 23 and May 3. Remote sensing measurements were taken within one hour of solar noon to minimize variation in illumination and solar zenith angle (Gu et al., 1992). Flights were executed using a spline survey in the DJIGO 4 application. The application ensured an altitude of 45 meters above ground level (AGL), an 80% front-lap, and 70% side-lap. A two-second timer and platform speed of 4.0 ms^{-1} allowed automated image collection using the Canon S110 while maintaining desired overlap for NIR imaging.

In 2019, data collection was executed on April 29th and May 17th, using the MicaSense RedEdge M multispectral sensor and severity ratings on May 3rd and May 17th. The May 3rd flight was executed under clear skies, near solar noon. The May 17th flight was executed under clear sky conditions approximately three hours before solar noon. The flights were executed

using a spline survey in the DJIGO 4 application that ensured an altitude of 30-meters AGL, an 80% image front-lap, 75% image side-lap, at 4.0 ms^{-1}, with the pixel size at approximately 1.8 cm. A Galaxy tablet (Samsung, Seoul, KOR) and an iPhone 7 Plus (Apple Inc., Cupertino, CA, USA) were used to launch the DJIGO 4 application and to monitor the multispectral sensor during data collection.

Images of the reflectance calibration panels were captured before and after flights to provide accurate reflectance data for each band. Green and yellow color disc panels were placed at the end of the field to serve as internal color standards for imaging across measurement days and lighting conditions for DGCI calculation (Fig. 2).

Mosaic Construction Using CMOS and Digital Sensor Data

For the 2018 data, a semi-automated processing pipeline was used to extract plot-level data from the UAS imagery (Haghighattalab et al., 2016). The Agisoft PhotoScan software (Agisoft LLC. St. Petersburg, RUS) was used to create mosaic images, using the scale-invariant feature transform (SIFT) algorithm (Lowe, 2004). The following workflow was used: (1) load the joint photographic experts group (JPEG) images, (2) image alignment, (3) import geo-referencing information, (4) build a dense point cloud, (5) build a dense elevation model (DEM) or Mesh, and (6) generate mosaics. After construction, mosaics were analyzed in the Field Analyzer software (https://www.turfanalyzer.com/field_analyzer.html) to determine DGCI and BNDVI of the individual plots

Mosaic Construction Using Multispectral Data

For the 2019 data, Pix4D Mapper Pro software (Pix4D S.A. Prilly, CHE) was used for image processing based on the SIFT algorithm. The following workflow was used: (1) import band

images (2) implement the Ag Multispectral processing template (3) insert radiometric calibration specifications and calibration panel images, and (4) process data. Spectral band images, including the geolocation and orientation data, were detected by Pix4D from the Exchangeable Image File (EXIF) metadata.

Reflectance panel data for each band was incorporated into the workflow and the calibrated reflectance surface was selected from each panel image by constructing a rectangular boundary around the surface. Albedo values for each band was set and radiometric correction was performed using the camera parameters and sun irradiance information in the EXIF metadata.

For final processing, the following workflow was used: (1) build a dense point cloud and mesh, (2) build a digital surface model (DSM), and (3) build mosaic and index reflectance maps. After processing in Pix4D, the mosaics and reflectance maps were exported as individual Geolocation Tagged Image File Formats (GeoTIFFs) for each band. These were imported into QGIS 3.8.0 (QGIS Development Team, 2019) to create a virtual raster layer for each measurement day, which QGIS recognized as a multispectral image. Each band was assigned relative to the program's recognition (Band 1=Blue, Band 2=Green, Band 3= Red) and the smallest minimum and largest maximum were made identical for all bands to create a more visually uniform image. RGB images were imported into Field Analyzer for DGCI analysis and NDVI reflectance maps were generated in Pix4D and imported as GeoTIFF files into QGIS.

Vegetative Indices

DGCI is calculated using the average of the transformed hue saturation and brightness (HSB) values. HSB values are based on human perception of color, where hue is defined as the angle on

a continuous circular scale from 0° to 360° (0°=red, 60°=yellow, 120°=green, 180°=cyan, 240°=blue, 300°=magenta), saturation is the purity of the color from 0% (gray) to 100% (fully saturated), and brightness is relative lightness or darkness of the color from 0% (black) to 100% white) (Purcell et al., 2013). The dark green HSB transform is calculated as *Hue – 60/60,* so that hues of 60 and 120 would equal to dark green hue transforms of zero and one (Karcher and Richardson, 2003). Since lower saturation and brightness values correspond to darker green colors, *1 – saturation* and *1 – brightness* was used to calculate the dark green color transforms for saturation and brightness. Taking the average of transformed HSB values result in a single measure of dark green color ranging from zero to one, with higher values corresponding to dark green color (Karcher and Richardson, 2003a). DGCI was calculated using this formula:

$$DGCI = [(Hue - 60)/60 + (1 - Saturation) + (1 - brightness)]/3$$

NDVI was calculated as the normalized transformed ratio between reflectance measurements at the red and NIR wavelength ranges:

$$NDVI = (NIR - RED) / (NIR + RED)$$

The RedEdge multispectral sensor provided 5-band TIFs with Red and NIR peaking at 668nm and 840nm wavelengths ("RedEdge-M User Manual (PDF),"). NDVI was calculated as a mean for each plot across all pixels. BNDVI was calculated as the normalized transformed ratio between reflectance measurements at the blue wavelength range and NIR wavelength range using this formula:

$$BNDVI = (NIR - BLUE) / (NIR + BLUE)$$

Where the NIR wavelength ranged from 700-900 nm and the blue and green wavelengths from 360-550 nm. BNDVI was also calculated as a mean for each plot.

DGCI and BNDVI values were calculated in Field Analyzer, creating polygons manually, capturing only the center (core) of the plot. For NDVI, uniform polygons 0.86 m in length and 0.10 m in width were placed over each plot using the grid creator plugin in QGIS. Zonal statistics were used to calculate the average NDVI across the pixels within each polygon.

Statistical Analysis

For the first year, in which a RCBD was used, each response variable was analyzed in an analysis of variance (ANOVA) and adjusted means were calculated using a mixed linear model in SAS 9.4 software (SAS Institute, Cary, NC):

$$Y_{ijk} = \mu + R_i + L_k + \square_{ijk}$$

where Y_{ijk} is the response variables relative to phenotypic observation, μ is the overall mean, R_i is the random replication effect of the i^{th} replication, L_k is the fixed genotype effect of the k^{th} genotype, and $\square_{ijk}$ is the random error term. For the augmented design used in year two, the following formula was used for ANOVA:

$$Y_{ijk} = \mu + \beta_i + C_j + L_{k(i)} + \square_{ijk.}$$

where Y_{ijk} is the response variables relative to the phenotypic observation, μ is the overall mean, β_i is the random block effect of the i^{th} block, C_j is the fixed controls effect of the j^{th} resistant and susceptible check, $L_{k(i)}$ is the k^{th} genotype nested within each block, and $\square_{ijkl}$ is the random error term. When data were combined across years, the following formula was used:

$$Y_{ijkl} = \mu + L_k + Y_i + LY_{ik} + A_{l(k)} + R_{(j)} + \square_{ijkl}$$

where Y_{ijkl} is the response variables relative to the phenotypic observation, μ is the overall mean, L_k is the fixed genotypic effect of the k^{th} genotype, Y_i is the fixed year effect of the i^{th} year, LY_{ik} is

the fixed interaction effect of the genotype by year interaction, $A_{l(k)}$ is the fixed awns effect of the l^{th} presence or absence of awns nested within the genotype, $R_{j(i)}$ is the random replication effect of the j^{th} replication nested within the year, and $\square_{ijkl}$ is the random error term.

Linear regressions were used to assess the relationship between visual severity ratings and remote (DGCI and BNDVI) and proximal (NDVI) sensing data in JMP Pro 14.2 (SAS Institute, Cary, NC). For regressions, a negative slope would indicate the expected relationships between the modified Cobb scale and DGCI and NDVI.

Genome-Wide Association Study

The GAWN was previously analyzed using genotype by sequencing (GBS) at the United States Department of Agriculture Eastern Genotyping Lab in Raleigh, NC. DNA was extracted using a Mag-Bind® Plant DNA Plus kit from Omega Bio-tek, according to manufacturer's recommended protocol. GBS libraries were assimilated using Pst1-Msp1 in conjunction with the Pst1-Mse1 restriction enzymes. The samples were barcoded, pooled at 192-plex, and sequenced on an Illumina Hi-Seq 2500 sequencer (Illumina Inc., San Diego, CA, USA). Molecular markers and the combined phenotypic datasets over years were used in the Genomic Association and Prediction Integrated Tool (GAPIT) in R v3.5.5 software to conduct a genome wide association study (GWAS) using a Fixed and Random Model Circulatory Probability Unification Multi-locus model (FarmCPU). The GWAS was performed using 594 genotypes and 49,024 GBS single nucleotide polymorphisms (SNPs) to identify marker-trait associations (MTAs). Population structure was controlled with the first seven principle components, as they each accounted for more than two percent of the total genetic variation of the population.

Results

Analysis of Variance – Year One

In year one, the population had mean severity ratings of 15% at the heading stage and 42% at the ripening stage, indicating positive disease progression. The effect of genotype was significant for severity at booting, severity at heading, and DGCI at booting. The effect of awns was not significant when included in the model (Table 2). The strongest linear relationship was observed between severity and DGCI (R^2=0.55, p<0.0001) during grain-fill. Significant relationships were also observed between severity and DGCI (R^2=0.08, p<0.0001) at booting and severity and BNDVI (R^2=0.12, p<0.0001) during grain-fill. (Table 3. Fig.3)

Analysis of Variance – Year Two

In year two, the population had a mean severity rating of 7% at booting, 15% at heading, 30% during grain-fill, and an average AUDPC value of 91, indicating positive disease progression. The effect of genotype was significant (p<0.0001) for severity at heading, severity at grain-fill, Greenseeker at booting, Greenseeker at grain-fill, and DGCI at booting. (Table 1). Significant relationships were observed for severity and DGCI (R^2=0.13, p <0.0001) at booting, severity and DGCI (R^2 = 0.16, p<0.0001) during grain-fill, and severity and NDVI during grain-fill (R^2 = 0.36, p<0.0001) (Table 3). Both years followed a similar trend of stronger relationships between visual and remote measurements from latter flights (Fig 4). The strongest relationship between proximal (Greenseeker) and remote (UAS) measurements of NDVI was during grain-fill (R^2 = 0.42, p<0.0001).

Analysis of Variance – Combined Over Years

When data were combined across years, the effect of genotype was significant ($p<0.0001$) for severity at booting, severity at grain-fill, and DGCI at grain-fill. The interaction of year and genotype was significant for severity and DGCI during grain-fill. The effect of awns nested within genotype was significant for severity during grain-fill ($p<0.0001$) and DGCI during grain-fill ($p<0.05$) (Table. 2). The most significant linear relationship was observed between severity and DGCI ($R^2 = 0.58$, $p<0.0001$) at grain-fill. A significant relationship was also observed between severity and DGCI ($R^2 = 0.17$, $p<0.0001$) at the booting stage (Table 3, Fig. 5).

Confidence interval analysis at 95 % indicated that for any given plot with DGCI = 0.40, the prediction of a new individual would be between 61 % to 100 % severity. For DGCI = 0.50, the prediction of a new individual would be between 30 % and 100 %. For DGCI = 0.60, the predicted severity rating of a new individual ranged from 0% to 100 %. For DGCI = 0.70 DGCI, the predicted severity rating ranged from 0 to 70 %. For DGCI = 0.80, the predicted severity rating ranged from 0 % to 40 %.

Marker-Trait Associations for Stripe Rust Resistance

The FarmCPU model identified 28 MTAs that exceeded the Bonferroni corrected threshold of $-\log_{10}(p) \geq 5.99$ for the four response variables from the combined dataset (Table 5, Fig. 7 and 8). There were ten MTA for severity during booting, seven for severity during grain-fill, four for DGCI during booting, and six for DGCI during grain-fill. For the booting stage, MTAs for severity were identified on chromosomes 1B, 2A, 2B, 2D, 3A, 3B, 4B, 6B, 7A; with the most significant, SNP, S2A_18910313, located on chromosome 2A (Table 5). For DGCI at the booting stage, MTAs were identified on chromosomes 1B, 2A, 3D, and 5B; with

S5B_529987661 on 5B. Consistent MTAs across visual and remote measurements at the booting stage were located on chromosomes 1B and 2A (Table 5 Fig. 7).

At the grain-fill stage, MTAs for visual severity ratings were identified on the 2B, 3B, 4B, 6B, and 7A chromosomes; with the most significant SNP, S4B_598847646 on chromosome 4B (Table 5). For DGCI at grain-fill, MTAs were identified on chromosomes 2A, 4B, 6A, and 7D, with the most significant SNP, S4B_609487031, located on chromosome 4B (Table 5). A consistent MTA across visual and remote measurements during grain-fill was identified on chromosome 4B (Fig. 8).

Discussion

Relationship Between Visual Severity and Remote Sensing Indices

Significant linear relationships between visual severity and remote sensing indices, particularly DGCI, were observed across both years and in the combined analysis. In general, the severity ratings and DGCI at booting of each year had a weaker relationship (R^2 = 0.08 and 0.14 for year one and two, respectively) compared to latter flights, likely the result of lower disease pressure, leading to low visible differences between healthy and damaged leaf color at that time. As severity increased, the ability of the UAS to differentiate between severity levels improved and a stronger relationship was observed (R^2 = 0.55 and 0.16 for year one and two, respectively). The relationship also improved as more data were included in the regression model, as seen in the combined analysis (R^2 = 0.18 and 0.58 at booting and grain-fill stages respectively). The relationship between visual severity and BNDVI was generally weak in comparison to DGCI and the multispectral NDVI, likely due to the lack of image resolution and sensitivity of the index.

In year two, multispectral NDVI showed a stronger relationship with visual severity (R^2 = 0.36) compared to DGCI, possibly due to the sensitivity of NDVI to differentiate between healthy and stripe rust induced damage. Devadas et al (2009) evaluated the ability of several indices to distinguish stripe rust damage from that of leaf and stem rust in a controlled environment. They found that for the mean values of the vegetative indices, including NDVI, across all three rust pathogens, that stripe rust produced the strongest response due to the rapid generation of uredia per fungal colony developing streaks of yellow-orange color down the leaf and hindering the proper absorption of red wavelengths and reflectance of NIR. Su et al (2018) evaluated several narrow band indices for their ability to detect stripe rust in a field-based environment using UAS and multispectral imagery. They found NDVI to be the second most capable index among 22 narrow-band indices for detecting stripe rust. Both studies support the relationship observed in the current study.

A significant relationship between proximal and remote sensing measurements of NDVI (R^2 = 0.42 p<0.0001) was also observed, in agreement with other studies where R^2 = 0.63 to 0.84 have been reported (Arora et al., 2013; Duan et al., 2017). For the latter, seven-meter plot sizes were used, possibly influencing the relationship between proximal and remote NDVI. Using single-row plot sizes likely introduces error and reduces the strength of the relationship in our study. In addition, the spatial resolution of the multispectral sensor was approximately of 1.8 cm at 30m AGL, making it capable of sensing shadows, soil and underlying biomass within the field of view as previously reported by Lu and He (2018).

Predictability of Visual Severity

The linear predictability of visual severity ratings using DGCI was evaluated by analyzing the upper and lower limits at 95% confidence for the strongest relationship observed in the study

between visual severity and DGCI ($R^2 = 0.58$). The upper and lower confidence limits represent the range in severity for a new DGCI value of an un-replicated measurement. The mean upper and lower confidence limits represent the range of severity for a new mean DGCI value with three replicates. At a DGCI value of 0.40 the predicted severity ranges from 60% to 100%, while the mean confidence limits are 100% (Table 4). On the other end of the spectrum at a DGCI value of 0.80, the predicted severity ranges from 0% to 40%, while the mean confidence limits are 0%. Overall, when predicting visual severity, analyzing the mean of three replicates was more accurate compared to a single replicate. However, a DGCI value of 0.40 includes only 17% of the total genotypes. From a practical viewpoint, a breeder could successfully remove these susceptible genotypes using either the replicated or un-replicated design. In comparison, a DGCI value of 0.80 includes approximately 45% of the genotypes. Using an un-replicated design in this scenario would risk low accuracy or advancement of moderately susceptible genotypes. In addition, the average DGCI value showed no significant difference between a severity rating of 2% and 70% (Fig. 6). Although DGCI has not previously been used as an indirect measurement of disease severity, our results indicate that it does have utility in this area, despite some limitations. In general, there was a relationship, but the ability to predict visual severity ratings using DGCI was not precise for new individual; however, replicating the population three times or more, improves precision (Table 4).

Marker Trait Associations

Proximal and UAS remote sensing have been successful in the detection of QTL for morphological (Virlet et al., 2015) and transpiration improvements, disease resistance (Kumar et al., 2016; Pretorius et al., 2017; Stewart et al., 2019), abiotic stress tolerance (Condorelli et al., 2018), plant height (Wang et al., 2019; Hassan et al., 2019) and other traits. In the current study,

different MTAs were detected during early UAS flights and early visual ratings compared to latter assessments. Consistent MTAs identified during for visual ratings during the booting stage were located on chromosomes 1B and 2A. The 2A MTA is likely the resistance gene *Yr17*, introduced from *Aegilops ventricosa* chromosome 2NS and is widely present in US southern soft wheat germplasm due to tight linkage with leaf rust (*Lr37*), and stem rust resistance (*Sr38*) genes (Robert et al., 1999; Helguera et al., 2003). It has previously been classified as both an all-stage and adult plant resistance gene (Sthapit et al., 2011; Hubbard and Bayles, 2013; Milus et al., 2015). The MTA on chromosome 1B is likely the resistance gene Yr15, introduced from wild Emmer wheat, (*Triticum dicoccoides)* and previously reported to confer resistance to a broad spectrum of stripe rust isolates at both seedling and adult plant stages (Gerechter-Amitai et al., 1989; Peng et al., 2000).

For the visual and DGCI measurements during grain-fill, a consistent MTA was detected on chromosome 4B only. Previous research indicates that the 4B chromosome contains an APR gene with minor effects (William et al., 2003; Suenaga et al., 2003; Yang et al., 2016). Stripe rust resistance in the soft wheat cultivar 'USG3555' was mapped to the 4BS region (Christopher et al., 2013) and present in multiple soft red winter wheat genotypes. Overall these results indicate that UAS remote sensing can be a surrogate for traditional phenotyping in the identification of MTAs for stripe rust resistance.

Conclusion

As stripe rust virulence continues to evolve, so does the size and diversity of breeding programs, and the cost and labor for phenotyping. This research showed a relationship between visual stripe rust severity ratings and both DGCI and NDVI in a diverse population of wheat genotypes, though there are constraints that limit the confidence. Our results also indicate that the ability to

predict stripe rust severity using DGCI is not precise for predicting a genotype in an un-replicated design. However, precision does improve with replication. Lastly, the results show that although DGCI has not been used for assessing disease severity, it can identify resistance genes for stripe rust that are also detected when severity is rated visually. Further research is warranted on plot size, optimal spatial resolution, and extensively on NDVI or other specialized vegetative indices that could be more sensitive to stripe rust detection and less sensitive non disease related phenotypic variation.

Acknowledgments

We thank the Agriculture and Food Research Initiative Competitive Grant 2017-67007-25939 (Wheat-CAP) from the USDA National Institute of Food and Agriculture, the Arkansas Wheat Promotion Board, and the USDA Wheat and Barley Stripe Rust Initiative for financial support; Dr. L. Mozzoni, Dr. L Purcell, and Mr. Daniel Rogers for their assistance in providing the UASs and remote sensors used in this study.

References

Aparicio, N., D. Villegas, J. Casadesus, J.L. Araus, and C. Royo. 2000. Spectral vegetation indices as nondestructive tools for determining durum wheat yield. Agronomy Journal 92(1): 83–91.

Arguello, M.N., R.E. Mason, T.L. Roberts, N. Subramanian, A. Acuña, et al. 2016. Performance of soft red winter wheat subjected to field soil waterlogging: Grain yield and yield components. Field Crops Research 194: 57–64. doi: 10.1016/j.fcr.2016.04.040.

Arora, A., R.K. Sharma, M.S. Saharan, K. Venkatesh, N. Dilbaghi, et al. 2013. Quantifying stripe rust reactions in wheat using a handheld NDVI remote sensor. Proceedings of BGRI2013 Technical Workshop. p. 19–22

Bacon, R.K., J.T. Kelly, E.A. Milus, and C.E. Parsons. 2004. Registration of'Pat'wheat. Crop science 44(2): 694–696.

Carleton, M.A. 1915. Hard wheats winning their way. US Department of Agriculture.

Chen, X.M. 2005. Epidemiology and control of stripe rust [*Puccinia striiformis* f. sp. *tritici*] on wheat. Canadian Journal of Plant Pathology 27(3): 314–337. doi: 10.1080/07060660509507230.

Chen, X.M. 2007. Challenges and solutions for stripe rust control in the United States. Australian Journal of Agricultural Research 58(6): 648–655.

Chen, X., M. Moore, E.A. Milus, D.L. Long, R.F. Line, et al. 2002. Wheat stripe rust epidemics and races of Puccinia striiformis f. sp. Tritici in the United States in 2000. Plant Disease 86(1): 39–46. doi: 10.1094/PDIS.2002.86.1.39.

Chen, X., L. Penman, A. Wan, and P. Cheng. 2010. Virulence races of Puccinia striiformis f. sp. tritici in 2006 and 2007 and development of wheat stripe rust and distributions, dynamics, and evolutionary relationships of races from 2000 to 2007 in the United States. Canadian Journal of Plant Pathology 32(3): 315–333. doi: 10.1080/07060661.2010.499271.

Cheng, P., L.S. Xu, M.N. Wang, D.R. See, and X.M. Chen. 2014. Molecular mapping of genes Yr64 and Yr65 for stripe rust resistance in hexaploid derivatives of durum wheat accessions. Theor Appl Genet 127(10): 2267–2277. doi: 10.1007/s00122-014-2378-8.

Christopher, M.D., S. Liu, M.D. Hall, D.S. Marshall, M.O. Fountain, et al. 2013. Identification and mapping of adult-plant stripe rust resistance in soft red winter wheat cultivar 'USG 3555.' Plant Breeding 132(1): 53–60. doi: 10.1111/pbr.12015.

Condorelli, G., M. Maccaferri, M. Newcomb, P. Andradre-Sanchez, W.W. Jeffrey, et al. 2018. Comparative aerial and ground based high throughput phenotyping for the genetic dissection of NDVI as a proxy for drought adaptive traits in durum wheat. Frontiers in Plant Science. doi: 10.3389/fpls.2018.00893.

Devadas, R., D.W. Lamb, S. Simpfendorfer, and D. Backhouse. 2009. Evaluating ten spectral vegetation indices for identifying rust infection in individual wheat leaves. Precision Agriculture; Dordrecht 10(6): 459–470. doi: http://0-dx.doi.org.library.uark.edu/10.1007/s11119-008-9100-2.

Duan, T., S.C. Chapman, Y. Guo, and B. Zheng. 2017. Dynamic monitoring of NDVI in wheat agronomy and breeding trials using an unmanned aerial vehicle. Field Crops Research 210: 71–80.

Gerechter-Amitai, Z.K., C.H. Van Silfhout, A. Grama, and F. Kleitman. 1989. Yr15—a new gene for resistance to Puccinia striiformis in Triticum dicoccoides sel. G-25. Euphytica 43(1–2): 187–190.

Gu, X.F., G. Guyot, and M. Verbrugghe. 1992. Evaluation of measurement errors in ground surface reflectance for satellite calibration. International Journal of Remote Sensing 13(14): 2531–2546.

Haghighattalab, A., L.G. Perez, S. Mondal, D. Singh, D. Schinstock, et al. 2016. Application of unmanned aerial systems for high throughput phenotyping of large wheat breeding nurseries. Plant Methods; London 12. doi: http://0-dx.doi.org.library.uark.edu/10.1186/s13007-016-0134-6.

Hassan, M.A., M. Yang, L. Fu, A. Rasheed, B. Zheng, et al. 2019. Accuracy assessment of plant height using an unmanned aerial vehicle for quantitative genomic analysis in bread wheat. Plant Methods 15. doi: 10.1186/s13007-019-0419-7.

Heege, H.J., S. Reusch, and E. Thiessen. 2008. Prospects and results for optical systems for site-specific on-the-go control of nitrogen-top-dressing in Germany. Precision Agriculture 9(3): 115–131.

Helguera, M., I.A. Khan, J. Kolmer, D. Lijavetzky, L. Zhong-qi, et al. 2003. PCR assays for the Lr37-Yr17-Sr38 cluster of rust resistance genes and their use to develop isogenic hard red spring wheat lines. Crop Science 43(5): 1839–1847. doi: 10.2135/cropsci2003.1839.

Hubbard, A.J., and R.A. Bayles. 2013. UK cereal pathogen virulence survey, Yellow rust of wheat–2012 annual report. NIAB, Cambridge, England.

Jenkins, D., and B. Vasigh. 2013. Association for unmanned vehicle systems international. The economic impact of unmanned aircraft systems integration in the United States.

Karcher, D.E., and M.D. Richardson. 2003a. Quantifying turfgrass color using digital image analysis. Crop Science 43(3): 943–951. doi: 10.2135/cropsci2003.9430.

Karcher, D.E., and M.D. Richardson. 2003b. Quantifying turfgrass color using digital image analysis. Crop Science; Madison 43(3): 943–951.

Knipling, E.B. 1970. Physical and physiological basis for the reflectance of visible and near-infrared radiation from vegetation. Remote sensing of environment 1(3): 155–159.

Kumar, S., M.S. Röder, R.P. Singh, S. Kumar, R. Chand, et al. 2016. Mapping of spot blotch disease resistance using NDVI as a substitute to visual observation in wheat (Triticum aestivum L.). Molecular Breeding; Dordrecht 36(7): 1–11. doi: http://0-dx.doi.org.library.uark.edu/10.1007/s11032-016-0515-6.

Lan, C., G.M. Rosewarne, R.P. Singh, S.A. Herrera-Foessel, J. Huerta-Espino, et al. 2014. QTL characterization of resistance to leaf rust and stripe rust in the spring wheat line Francolin#1. Mol Breeding 34(3): 789–803. doi: 10.1007/s11032-014-0075-6.

Line, R.F. 2002. Stripe rust of wheat and barley in North America: A retrospective historical review. Annual Review of Phytopathology; Palo Alto 40: 75.

Liu, W., M. Frick, R. Huel, C.L. Nykiforuk, X. Wang, et al. 2014. The stripe rust resistance gene Yr10 encodes an evolutionary-conserved and unique CC–NBS–LRR sequence in wheat. Molecular plant 7(12): 1740–1755.

Long, L., F. Yao, C. Yu, X. Ye, Y. Cheng, et al. 2019. Genome-wide association study for adult-plant resistance to stripe rust in Chinese wheat landraces (Triticum aestivum L.) from the yellow and Huai river valleys. Front. Plant Sci. 10. doi: 10.3389/fpls.2019.00596.

Lowe, D.G. 2004. Distinctive image features from scale-invariant keypoints. International Journal of Computer Vision 60(2): 91–110.

Lu, B., and Y. He. 2018. Optimal spatial resolution of Unmanned Aerial Vehicle (UAV)-acquired imagery for species classification in a heterogeneous grassland ecosystem. GIScience & Remote Sensing 55(2): 205–220. doi: 10.1080/15481603.2017.1408930.

Ma, J., R. Zhou, Y. Dong, L. Wang, X. Wang, et al. 2001. Molecular mapping and detection of the yellow rust resistance gene Yr26 in wheat transferred from Triticum turgidum L. using microsatellite markers. Euphytica 120(2): 219–226. doi: 10.1023/A:1017510331721.

Madden, L.V., G. Hughes, and F. Van Den Bosch. 2007. The study of plant disease epidemics.

Marshall, D.M., R.K. Barnhart, S.B. Hottman, E. Shappee, and M.T. Most. 2016. Introduction to unmanned aircraft systems. Crc Press.

Milus, E.A., D.E. Moon, and R.E. Mason. 2015. Race-Specific Adult-Plant Resistance in Winter Wheat to Stripe Rust and Characterization of Pathogen Virulence Patterns | Phytopathology. https://apsjournals.apsnet.org/doi/full/10.1094/PHYTO-11-14-0305-R (accessed 3 September 2019).

Milus, E.A., E. Seyran, and R. McNew. 2006. Aggressiveness of Puccinia striiformis f. sp. tritici isolates in the South-Central United States. Plant Disease 90(7): 847–852. doi: 10.1094/PD-90-0847.

Peng, J.H., T. Fahima, M.S. Röder, Q.Y. Huang, A. Dahan, et al. 2000. High-density molecular map of chromosome region harboring stripe-rust resistance genes YrH52 and Yr15 derived from wild emmer wheat, Triticum dicoccoides. Genetica 109(3): 199–210.

Peterson, R.F., A.B. Campbell, and A.E. Hannah. 1948. A diagrammatic scale for estimating rust intensity on leaves and stems of cereals. Canadian journal of research 26(5): 496–500.

Pretorius, Z.A., C.X. Lan, R. Prins, V. Knight, N.W. Mclaren, et al. 2017. Application of remote sensing to identify adult plant resistance loci to stripe rust in two bread wheat mapping populations. Precision Agriculture; Dordrecht 18(4): 411–428. doi: http://0-dx.doi.org.library.uark.edu/10.1007/s11119-016-9461-x.

Purcell, L.C., R.L. Rorie, and D.E. Karcher. 2013. System and method of determining nitrogen levels from a digital image.

QGIS Development Team. 2019. QGIS Geographic Information System. Open Source Geospatial Foundation Project.

Rahmatov, M., M.S. Hovmøller, K. Nazari, S.C. Andersson, B.J. Steffenson, et al. 2017. Seedling and Adult Plant Stripe Rust Resistance in Diverse Wheat–Alien Introgression Lines. Crop Science 57(4): 2032. doi: 10.2135/cropsci2016.08.0664.

Reagan, J. 2017. Agriculture drone market may exceed $4 billion. DroneLife. https://dronelife.com/2017/10/05/report-agriculture-drone-market-may-exceed-4-billion/ (accessed 21 October 2019).

RedEdge-M User Manual (PDF). MicaSense Knowledge Base. http://support.micasense.com/hc/en-us/articles/115003537673-RedEdge-M-User-Manual-PDF- (accessed 22 October 2019).

Reynolds, M.P., C.S. Pierre, A.S.I. Saad, M. Vargas, and A.G. Condon. 2007. Evaluating potential genetic gains in wheat associated with stress-adaptive trait expression in elite genetic resources under drought and heat stress. Crop Science; Madison 47: S172–S189.

Robert, O., C. Abelard, and F. Dedryver. 1999. Identification of molecular markers for the detection of the yellow rust resistance gene Yr17 in wheat. Molecular Breeding 5(2): 167–175. doi: 10.1023/A:1009672021411.

Rorie, R.L., L.C. Purcell, M. Mozaffari, D.E. Karcher, C.A. King, et al. 2011. Association of "greenness" in corn with yield and leaf nitrogen concentration. Agronomy Journal; Madison 103(2): 529–535.

Rutkoski, J.E., J.A. Poland, R.P. Singh, J. Huerta-Espino, S. Bhavani, et al. 2014. Genomic selection for quantitative adult plant stem rust resistance in wheat. The Plant Genome 7(3). doi: 10.3835/plantgenome2014.02.0006.

Singh, R.P., J. Huerta-Espino, S. Bhavani, S.A. Herrera-Foessel, D. Singh, et al. 2011. Race non-specific resistance to rust diseases in CIMMYT spring wheats. Euphytica 179(1): 175–186. doi: 10.1007/s10681-010-0322-9.

Singh, R.P., P.K. Singh, J. Rutkoski, D.P. Hodson, X. He, et al. 2016. Disease impact on wheat yield potential and prospects of genetic control. Annual Review of Phytopathology 54: 303–322.

Stewart, E., T. Wiesner-Hanks, N. Kaczmar, C. DeChant, H. Wu, et al. 2019. Quantitative phenotyping of northern leaf blight in UAV images using deep learning. MDPI. https://doi.org/10.3390/rs11192209 (accessed 4 December 2019).

Sthapit, J., E.E. Gbur, G. Brown-Guedira, D.S. Marshall, and E.A. Milus. 2011. Characterization of resistance to stripe rust in contemporary cultivars and lines of winter wheat from the eastern United States. Plant Disease 96(5): 737–745. doi: 10.1094/PDIS-07-11-0612.

Stubbs, R.W. 1985. 3 - Stripe Rust. In: Roelfs, A.P. and Bushnell, W.R., editors, Diseases, Distribution, Epidemiology, and Control. Academic Press. p. 61–101

Su, J., C. Liu, M. Coombes, X. Hu, C. Wang, et al. 2018. Wheat yellow rust monitoring by learning from multispectral UAV aerial imagery. Computers and Electronics in Agriculture 155: 157–166. doi: 10.1016/j.compag.2018.10.017.

Suenaga, K., R.P. Singh, J. Huerta-Espino, and H.M. William. 2003. Microsatellite markers for genes Lr34/Yr18 and other quantitative trait loci for leaf rust and stripe rust resistance in bread wheat. Phytopathology 93(7): 881–890. doi: 10.1094/PHYTO.2003.93.7.881.

USDA, A. 2016. Small grain losses due to rust : USDA ARS. https://www.ars.usda.gov/midwest-area/stpaul/cereal-disease-lab/docs/small-grain-losses-due-to-rust/small-grain-losses-due-to-rust/ (accessed 9 July 2019).

Virlet, N., E. Costes, S. Martinez, J.-J. Kelner, and J.-L. Regnard. 2015. Multispectral airborne imagery in the field reveals genetic determinisms of morphological and transpiration traits of an apple tree hybrid population in response to water deficit. J Exp Bot 66(18): 5453–5465. doi: 10.1093/jxb/erv355.

Wang, X., R. Zhang, W. Song, L. Han, X. Liu, et al. 2019. Dynamic plant height QTL revealed in maize through remote sensing phenotyping using a high-throughput unmanned aerial vehicle (UAV) | Scientific Reports. https://www.nature.com/articles/s41598-019-39448-z (accessed 4 December 2019).

Wanjura, D.F., and J.L. Hatfield. 1987. Sensitivity of spectral vegetative indices to crop biomass. Transactions of the ASAE 30(3): 810–0816.

Wegulo, S.N., and E. Byamukama. 2012. Rust Diseases of Wheat. NebGuide, University of Nebraska- Lincoln (Plant Disease Wheat). http://extensionpublications.unl.edu/assets/html/g2180/build/g2180.htm#target4 (accessed 9 July 2019).

White, J.W., P. Andrade-Sanchez, M.A. Gore, K.F. Bronson, T.A. Coffelt, et al. 2012. Field-based phenomics for plant genetics research. Field Crops Research 133: 101–112. doi: 10.1016/j.fcr.2012.04.003.

Wiegand, C.L., A.J. Richardson, and P.R. Nixon. 1986. Spectral components analysis: a bridge between spectral observations and agrometeorological crop models. IEEE transactions on geoscience and remote sensing (1): 83–89.

William, M., R.P. Singh, J. Huerta-Espino, S.O. Islas, and D. Hoisington. 2003. Molecular Marker Mapping of Leaf Rust Resistance Gene *Lr46* and Its Association with Stripe Rust Resistance Gene *Yr29* in Wheat. Phytopathology 93(2): 153–159. doi: 10.1094/PHYTO.2003.93.2.153.

Wu, X.-L., J.-W. Wang, Y.-K. Cheng, X.-L. Ye, W. Li, et al. 2016. Inheritance and molecular mapping of an all-stage stripe rust resistance gene derived from the chinese common wheat landrace "Yilongtuomai." Journal of Heredity 107(5): 463–470. doi: 10.1093/jhered/esw032.

Yang, E., G. Li, L. Li, Z. Zhang, W. Yang, et al. 2016. Characterization of stripe rust resistance genes in the wheat cultivar Chuanmai45. Int J Mol Sci 17(4). doi: 10.3390/ijms17040601.

Tables and Figures

Table 1. Analysis of variance for genotype effect stripe rust severity and UAS measurements in 596 wheat genotypes evaluated over two growing seasons in Fayetteville, AR.

Year	**Response Variable**	**Genotype P-value**
2017-2018	Severity at booting	<0.0001
	Severity at grain-fill	<0.0001
	DGCI at booting	0.0391
	DGCI at grain-fill	0.8225
	BNDVI at grain-fill	0.8224
2018-2019	Severity at booting	0.1371
	Severity at heading	<0.0001
	Severity at grain-fill	<0.0001
	DGCI at booting	0.0183
	DGCI at grain-fill	0.4595
	NDVI at booting	0.7984
	NDVI at grain-fill	0.6643
	Greenseeker at booting	0.0370
	Greenseeker at heading	0.9453
	Greenseeker at grain-fill	<0.0001

Table 2. Combined analysis of variance for stripe rust severity and UAS measurements in 596 wheat genotypes evaluated over two growing seasons in Fayetteville, AR.

	P-value			
Response Variable	**Genotype**	**Year**	**Genotype by year**	**Awns**
Severity at booting	<0.0001	0.6499	1.0000	-
Severity at grain-fill	<0.0001	0.1190	<0.0001	0.3620
DGCI at booting	0.9997	0.1770	1.0000	-
DGCI at grain-fill	<0.0001	0.3770	<0.0001	0.0349

Awn measurements were not included due to the lack of awn presence during the booting stage.

Table 3. Linear regressions for stripe rust severity and UAS measurements in 596 wheat genotypes evaluated over two growing seasons in Fayetteville, AR.

Year	**Regression**	**R^2**	**P-value**
2017-2018	Severity x DGCI at booting	0.08	<0.0001
	Severity x DGCI at grain-fill	0.55	<0.0001
	Severity x BNDVI at grain-fill	0.12	<0.0001
2018-2019	Severity x DGCI at booting	0.14	<0.0001
	Severity x DGCI at grain-fill	0.16	<0.0001
	Severity x NDVI at grain-fill	0.37	<0.0001
	Severity x NDVI at booting	-0.0012	0.6101
	Greenseeker x NDVI at grain-fill	0.42	<0.0001
	Greenseeker x NDVI at booting	0.0002	0.7692
Combined	Severity x DGCI at booting	0.18	<0.0001
	Severity x DGCI at grain-fill	0.58	<0.0001

Table 4. Severity predictions using DGCI ratings of the combined data during the grain-fill evaluations at 95% confidence.

□DGCI	Prediction	□Std Err Pred.	□LCLI	◊UCLI	†LCLM	‡UCLM
0.40	113.354	5.50295	61.217	>100	> 100	>100
0.50	82.161	5.21810	30.137	>100	71.927	92.395
0.60	50.968	5.06846	<0	>100	41.027	60.909
0.70	19.776	5.06602	<0	71.742	9.840	29.712
0.80	-11.417	5.21099	<0	40.604	<0	<0

□DGCI: A given Dark Green Color Index
□Std Error Pred: The standard error of the predicted value
□LCLI: Lower confidence limit for a new predicted individual
◊UCLI: Upper confidence limit for a new predicted individual
†LCLM: Lower confidence limit for means
‡UCLM: Upper confidence limit for means

Table 5. Marker-trait associations (MTAs) identified by a FarmCPU model genome-wide association study for stripe rust severity and UAS measurements in 596 wheat genotypes evaluated over two growing seasons in Fayetteville, AR.

Response	SNP_Position	Chr	Allele	MAF†	P-value	Effect
Severity at booting	S2A_18910313	2A	T/C	0.47	7.6E-15	-3.55
	S1B_683140161	1B	T/C	0.05	1.92E-11	-5.48
	S4B_602447901	4B	C/T	0.41	1.59E-09	3.02
	S6B_591265094	6B	A/G	0.25	6.03E-09	2.73
	S2D_50157935	2D	G/C	0.05	4.62E-08	4.16
	S3B_650829511	3B	C/T	0.33	1.44E-07	-2.04
	S2B_666629276	2B	C/G	0.05	1.75E-07	4.07
	S3A_644716732	3A	C/T	0.07	2.15E-07	-3.32
	S2B_468445975	2B	G/A	0.27	2.55E-07	8.54
	S3B_7153553	3B	T/C	0.06	9.04E-07	-3.27
	S4B_580353549	4B	A/G	0.20	2.11E-06	2.37
	S4A_168336979	4A	G/A	0.07	3.2E-06	-2.99
	S7A_70208434	7A	T/C	0.06	4.34E-06	-2.75
	S6A_12087708	6A	T/C	0.05	7.45E-06	-3.29
	S4B_560999693	4B	C/T	0.24	1.46E-05	1.97
	S5A_700116990	5A	G/A	0.06	1.86E-05	-3.14
	S4A_717462504	4A	C/G	0.06	3.15E-05	-2.61
Severity at grain-fill	S4B_598847646	4B	C/T	0.38	1.84E-30	-12.56
	S3B_5973360	3B	A/G	0.26	4.45E-15	7.10
	S2B_468445975	2B	G/A	0.27	2.88E-08	21.66
	S2B_19375915	2B	A/C	0.46	3.29E-08	5.69
	S7A_636168477	7A	C/G	0.08	4.98E-07	6.95
	S6B_560457640	6B	A/G	0.28	6.68E-07	5.26
	S7A_726771085	7A	C/T	0.41	1.22E-06	-3.18
	S3B_361671302	3B	G/A	0.06	1.59E-06	8.679
	S5A_471182188	5A	A/C	0.07	3.01E-06	6.55
	S5B_265722985	5B	C/T	0.06	7.23E-06	-8.29
	S2A_11194997	2A	T/C	0.25	1E-05	-4.50
	S1A_519860957	1A	C/T	0.08	1.01E-05	-6.29
	S3B_589641918	3B	G/A	0.05	1.78E-05	9.04
	S4D_6558263	4D	A/G	0.34	1.9E-05	-3.30
	S2B_715023997	2B	A/G	0.31	2.92E-05	-4.32
	S4D_472982770	4D	G/A	0.27	7.63E-05	-3.68
DGCI at booting	S5B_529987661	5B	A/T	0.46	9.43E-08	0.01
	S2A_11194972	2A	A/G	0.48	2.06E-07	-0.01
	S3D_604968955	3D	A/G	0.16	2.13E-07	0.01
	S1B_281684193	1B	G/T	0.06	2.97E-07	0.01
	S3B_13454494	3B	C/G	0.41	1.05E-06	0.01
	S7A_693685823	7A	C/T	0.36	4.08E-06	-0.01
	S5B_268892901	5B	T/A	0.05	1.52E-05	0.01
	S3B_482345832	3B	C/T	0.19	1.68E-05	0.01

Table 5. (Cont.)

Response□	SNP_Position□	Chr□	Allele	MAF†	P-value	Effect
	S2B_34843162	2B	G/C	0.05	4.3E-05	-0.01
	S1A_3780088	1A	T/C	0.28	5.01E-05	0.01
	S7A_643418804	7A	T/C	0.41	5.45E-05	-0.004
	S3A_37498804	3A	G/T	0.26	5.8E-05	-0.01
	S2B_217268814	2B	T/C	0.06	7.58E-05	-0.01
DGCI at grain-fill	S4B_609487031	4B	T/C	0.48	6.93E-15	0.02
	S2A_3634514	2A	C/T	0.48	8.09E-09	0.01
	S7D_388736851	7D	A/C	0.22	4.23E-08	-0.01
	S4B_580353549	4B	A/G	0.21	7.88E-08	-0.01
	S6A_2997672	6A	A/G	0.15	2.86E-07	0.01
	S2A_11552559	2A	A/G	0.25	4.9E-07	-0.01
	S6A_456295876	6A	C/T	0.09	1.22E-06	-0.01
	S2B_488198528	2B	A/G	0.28	1.47E-06	0.03
	S7A_37923130	7A	C/T	0.27	2.5E-06	0.01
	S3A_627917290	3A	C/G	0.06	3.79E-06	0.01
	S3B_735391182	3B	T/C	0.10	4.66E-06	-0.01
	S7A_49510162	7A	C/G	0.23	6.78E-06	-0.01
	S5D_431083013	5D	A/C	0.06	7.68E-06	0.01
	S5B_268892901	5B	T/A	0.05	2.39E-05	0.02
	S3B_5973360	3B	A/G	0.26	3.56E-05	-0.01
	S1A_504420080	1A	G/C	0.26	7.8E-05	0.01

Response□: response variables including visual and remote sensing evaluations over measurement days
SNP□: *single-nucleotide polymorphism*
Chr□: Triticum aestivum chromosome number
MAF†: Minor allele frequency

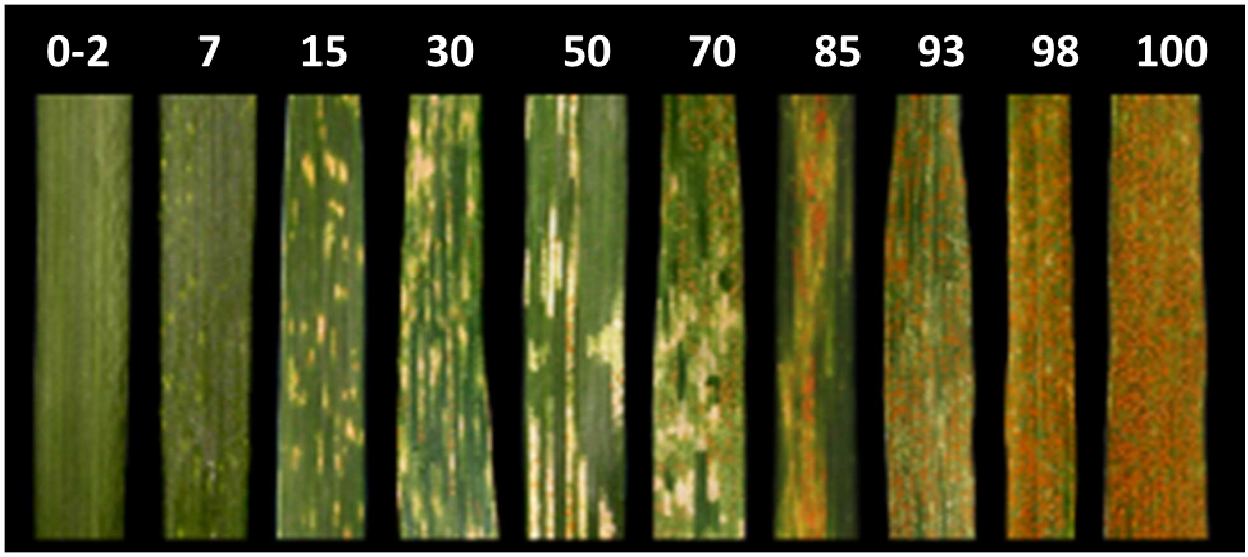

Figure 1: The Modified Cobb visual rating scale with severity ratings ranging from 0 to 100 based on the severity of stripe rust infection on the leaf.

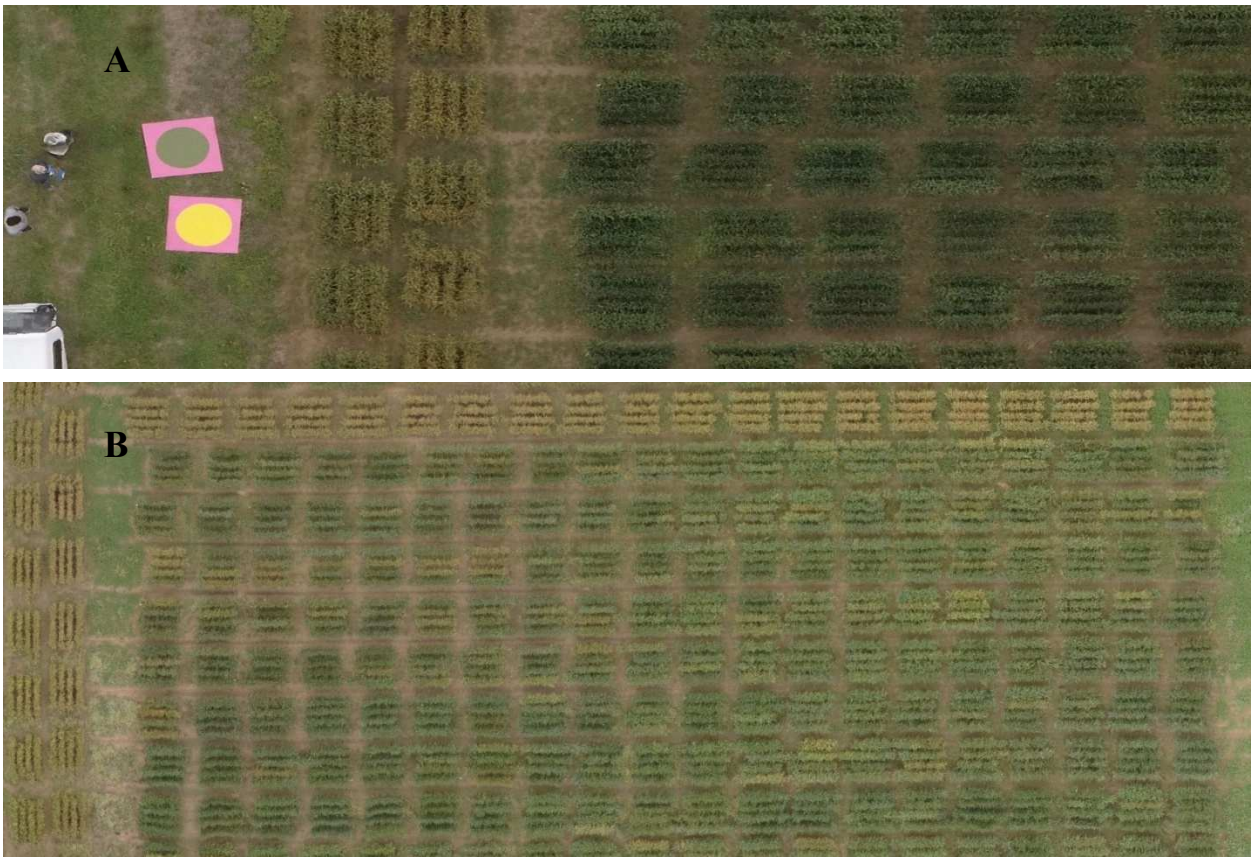

Figure 2: (A) Color standards placed at the end of the field. **(B)** RGB image at 45m AGL from the CMOS 20 Megapixel camera.

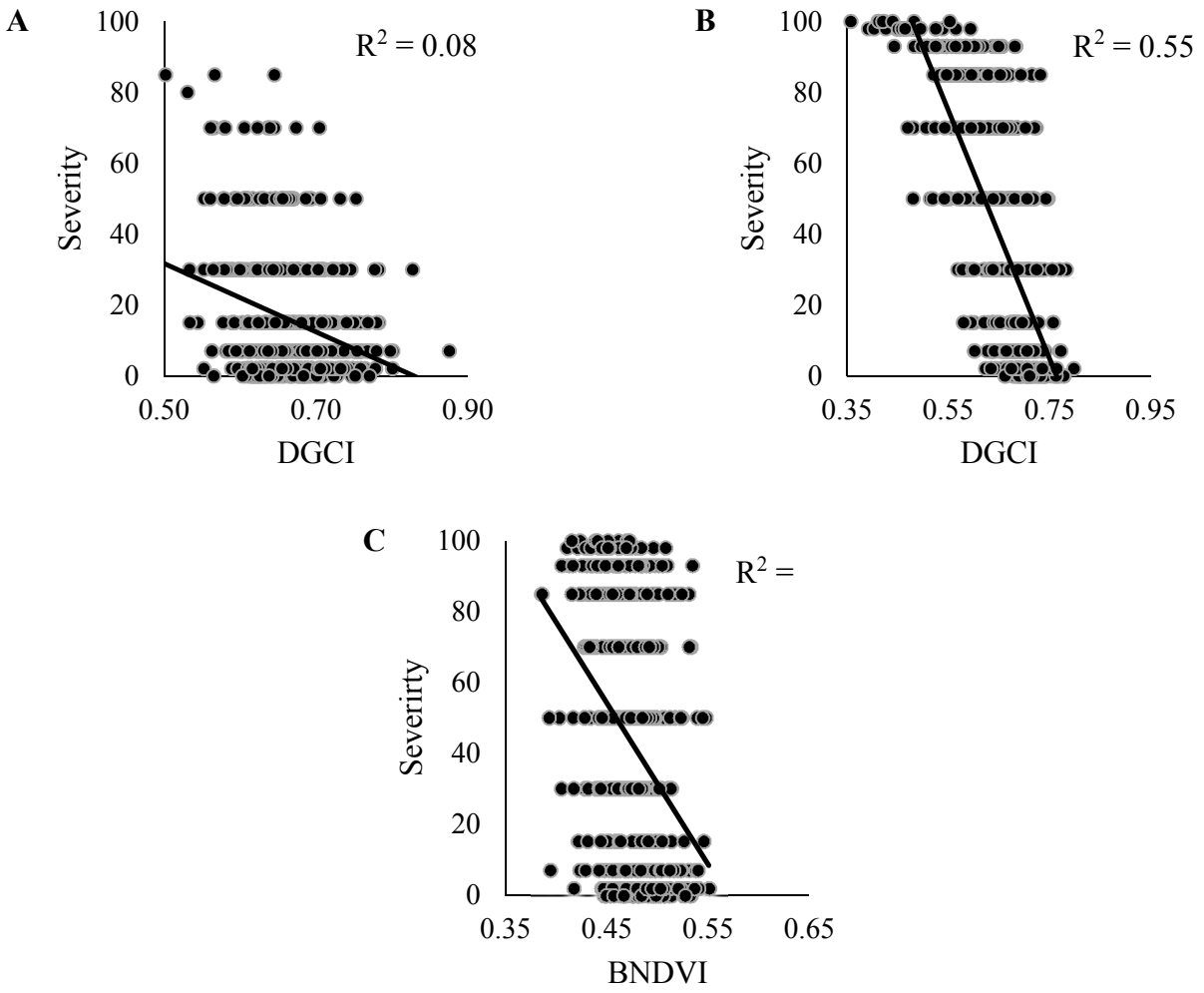

Figure 3: Linear Regressions in the 2017-2018 growing season. **A)** The relationship between the DGCI and visual severity evaluations during the booting stage. **B)** The relationship between the DGCI and visual severity evaluations during the grain-fill stage. **C)** The relationship between the blue NDVI and visual severity evaluations during the booting stage.

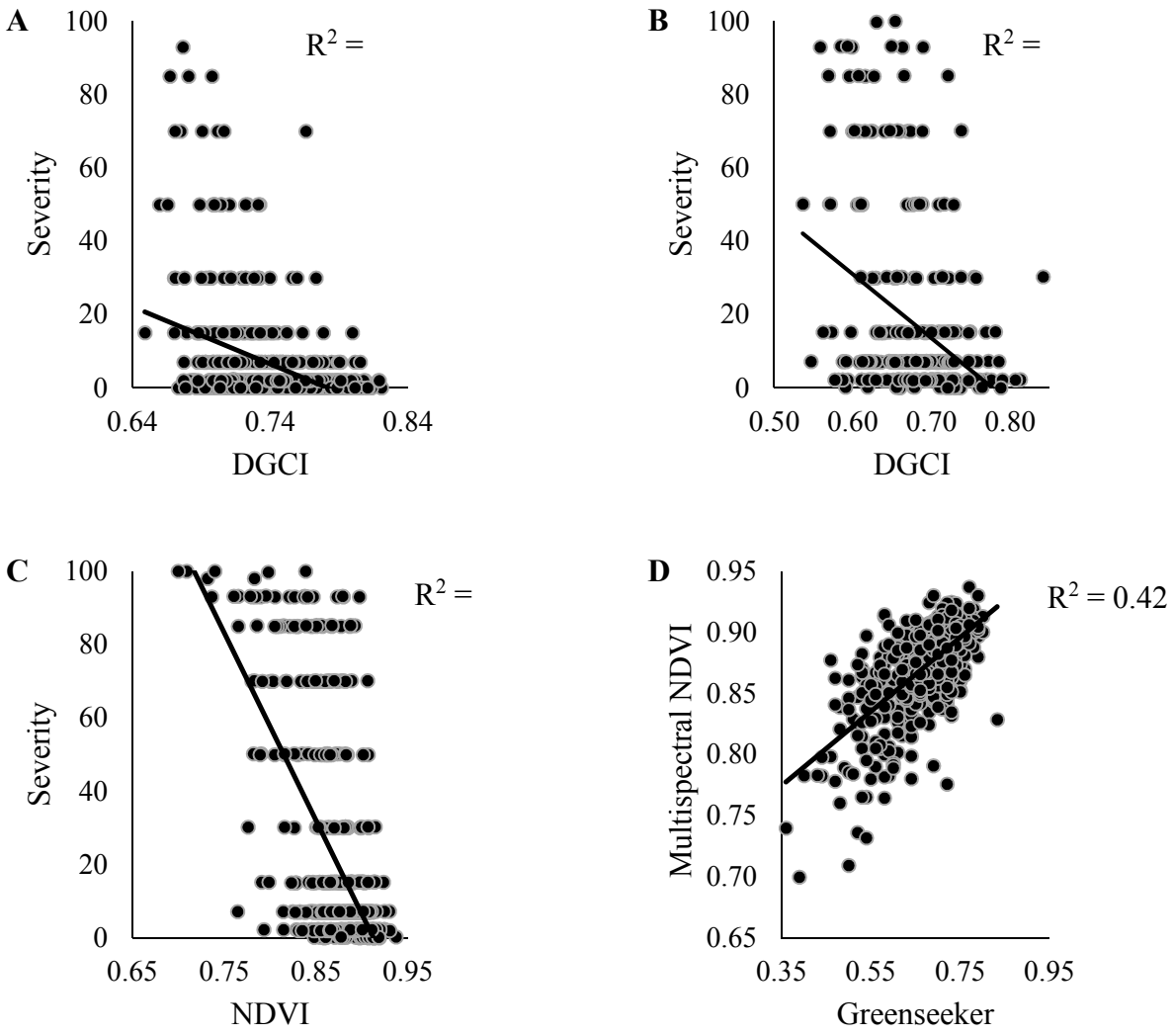

Figure 4: Linear Regressions in the 2018-2019 growing season. **A)** The relationship between the DGCI and the visual severity evaluations during the booting stage. **B)** The relationship between the DGCI and the visual severity evaluations at the grain-fill stage. **C)** The relationship between the NDVI and visual severity evaluations during the grain-fill stage. **D)** The relationship between the greenseeker and the multispectral NDVI evaluations during the grain-fill stage.

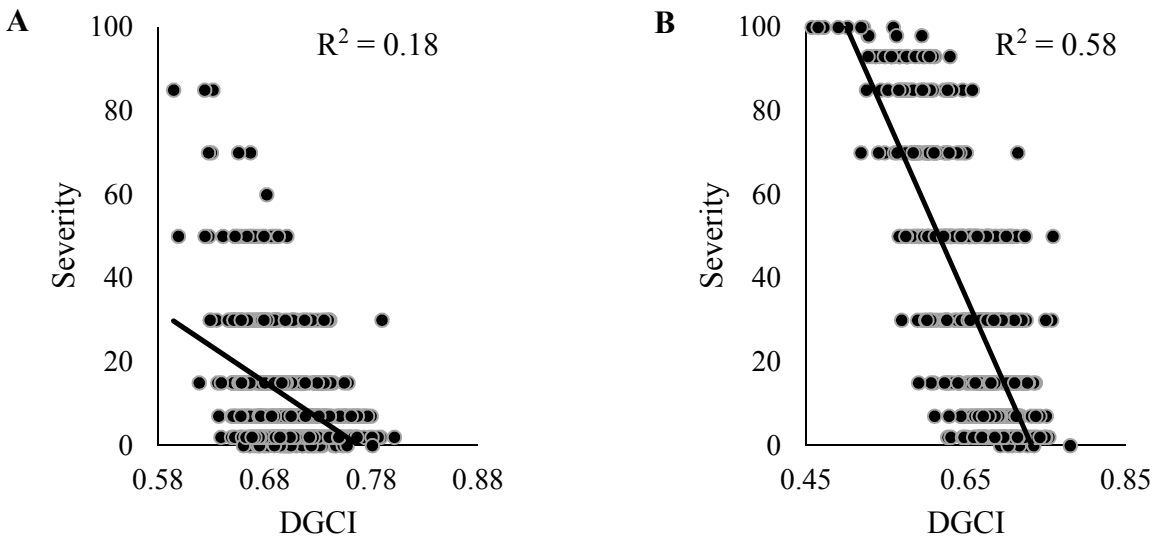

Figure 5: Linear Regressions of the combined data over both years. **A)** The relationship between the DGCI and visual severity evaluations during the booting stage. **B)** The relationship between the DGCI and visual severity evaluations during the grain-fill stage

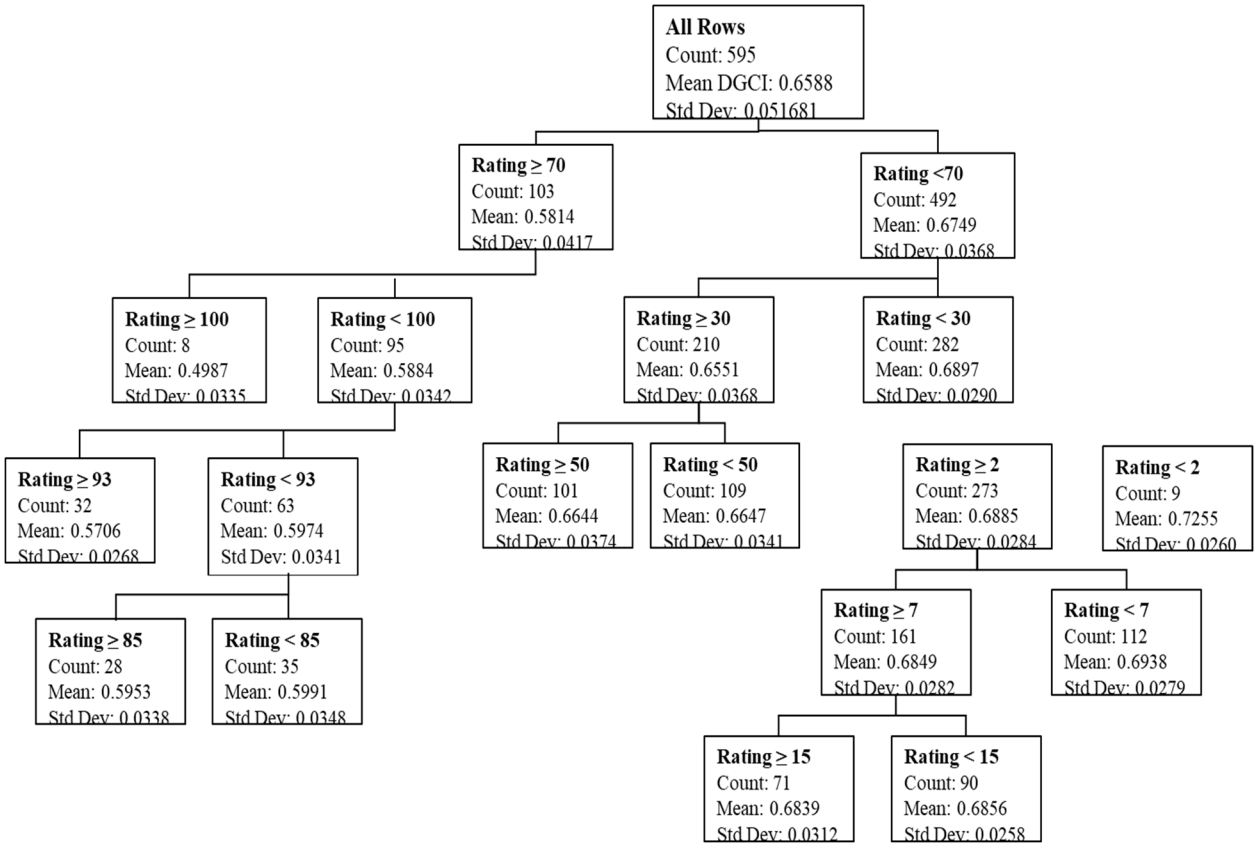

Figure 6: Predictive partitioning tree plot of the combined data, at the grain-fill stage, split by the modified Cobb rating scale with the number of lines, mean DGCI values, and standard deviation within each split.

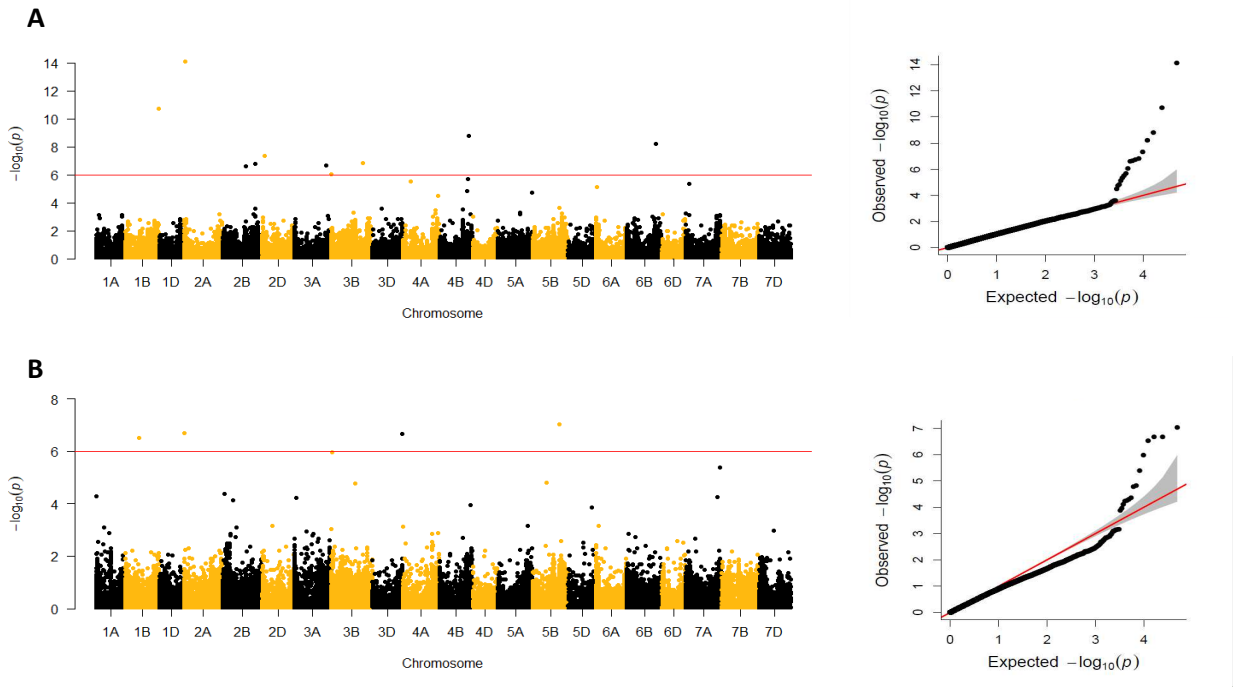

Figure 7: Manhattan plots and Quantile-Quantile Plots showing marker-trait associations identified in the Fixed and random model Circulatory Probability Unification (FarmCPU) model. (A) MTAs identified from the visual evaluations during the booting stage. (B) MTAs identified from the DGCI evaluations during the booting stage. The x-axis displays the respective chromosome and the y-axis displays the likelihood of odds (LOD) score. The red dashed line is the Bonferroni threshold set at a LOD=5.99 or p=0.00000102.

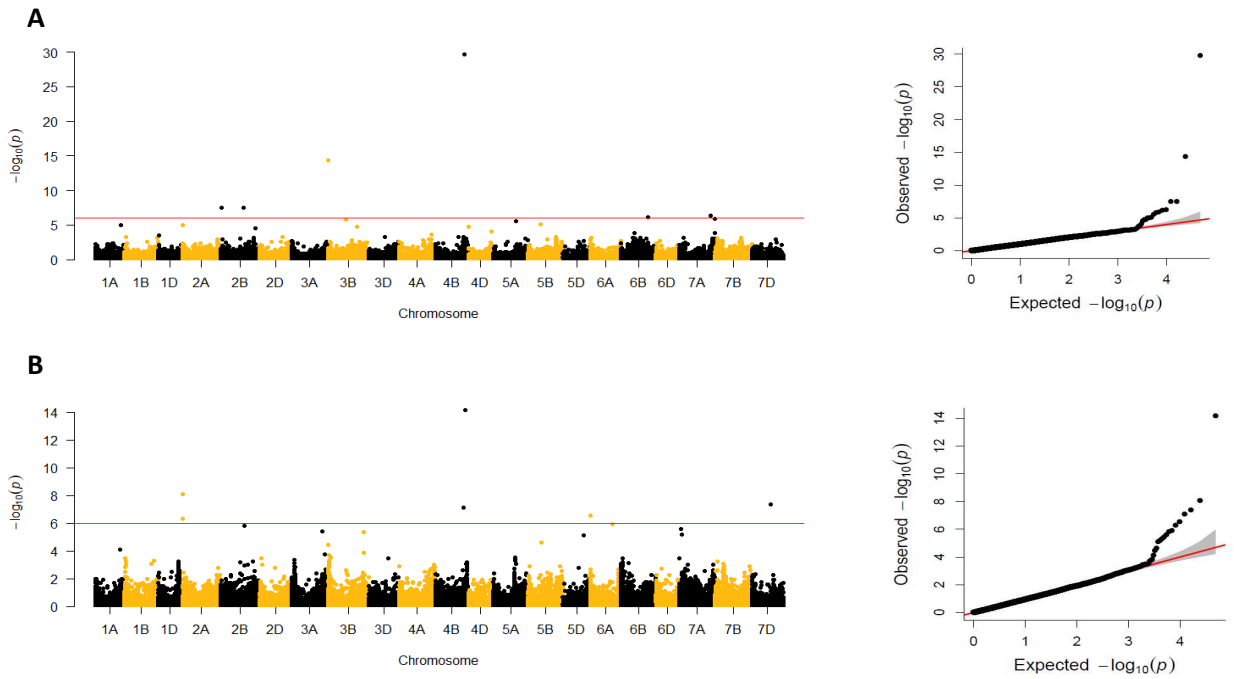

Figure 8: Manhattan plots and Quantile-Quantile plots showing marker-trait associations identified in the Fixed and random model Circulatory Probability Unification (FarmCPU) model (A) MTAs identified from visual evaluations during the grain-fill stage. (B) MTAs identified from the DGCI evaluations during the grain-fill stage. The x-axis displays the respective chromosome and the y-axis displays the likelihood of odds (LOD) score. The red dashed line is the Bonferroni threshold set at a LOD=5.99 or p=0.00000102.

CHAPTER 3: EVALUATING THE PLOT SIZE EFFECT ON THE RELATIONSHIPS BETWEEN VISUAL, PROXIMAL, AND REMOTE SENSING MEASUREMENTS FOR STRIPE RUST SEVERITY IN WHEAT

Abstract

Stripe rust (*Puccinia striiformis f. sp. Tritici)* is a foliar disease that significantly impacts global wheat production. When breeding for resistance, phenotyping large nurseries can be a bottleneck for genetic improvement. The use of unmanned aerial systems (UAS) for high-throughput phenotyping is on the rise, but their accuracy compared to manual ground measurements needs further proof of concept. Here, the effect of plot size (single-row, two-row, and four-row) on the ability of UAS to assess stripe rust severity in an inoculated nursery was explored in a panel of 13 genotypes preselected to range from 0 to 100 % severity. The normalized difference vegetation index (NDVI) and dark green color index (DGCI) were measured by UAS at the booting and grain-fill stages to determine their relationship with ground severity ratings. Significant (p<0.0001) relationships were observed between visual severity and DGCI across both measurement days, with the four-row plot size having the strongest relationship (R^2 = 0.84 to 0.85), though not significantly different from single-row (R^2 = 0.75 to 0.74) or two-row (R^2= 0.72 to 0.71). Significant regressions were also observed between visual severity and NDVI, where the two-row (R^2 = 0.78) and four-row (R^2 = 0.84) plot size regressions were significantly stronger than single-row (R^2 = 0.02) during the booting stage. Overall, this research provides evidence that larger plot sizes significantly increase the accuracy of sensor-based assessment of stripe rust severity in wheat using UAS.

Introduction

Stripe rust is a foliar disease of wheat (*Triticum aestivum)* caused by the fungal pathogen *Puccinia striiformis f. sp. Tritici*. It is one of the most devastating wheat diseases globally, reported in over 60 countries (Stubbs, 1985; Line, 2002; Chen, 2005; Chen et al., 2010). Yield losses of 50 to 100% have been reported with the most significant yield losses from infection occurring early in the growing season, in cool and wet conditions (Chen et al., 2002; Wegulo and Byamukama, 2012). In the US, stripe rust was first identified in Washington in 1915 and the first notable outbreak occurred during the 1950s in western Washington. (Carleton, 1915; Chen, 2007). The spread of stripe rust has resulted from new races of *P. striiformis* that have overcome deployed resistance genes, challenging wheat breeders and producers seasonally (Line, 2002; Chen et al., 2010).

Within the past decade, a lower cost for whole-genome sequencing and genotyping has resulted in a plethora of genomic information on disease resistance quantitative trait loci (QTL) (Jannink et al., 2010; Brachi et al., 2011). However, accurate phenotyping remains a vital component for genetic improvement, including for stripe rust resistance. The challenge for plant breeders now becomes producing phenotypic information to keep pace with genomics (Furbank and Tester, 2011; White et al., 2012). Phenotyping of single plots in large breeding nurseries is difficult and can have low accuracy when performed quickly. (Fehr, 1991; Andrade-Sanchez et al., 2014). High-throughput phenotyping, including both proximal and remote sensing, provides a potentially more rapid method to produce phenotypic data, (Poland and Price, 2015; Haghighattalab et al., 2016). However, to be useful in a practical breeding program high-throughput methods must be accurate within the context of varying plot sizes, experimental designs, and field conditions (Haghighattalab et al., 2016).

Proximal sensing is defined as a measurement taken in close range of the plants, resulting in less atmospheric interference. This is done using a hand-held sensor or a vehicle modified with sensors to provide high resolution and multiple view angles at a known distance (Ruixiu et al., 1989; Andrade-Sanchez et al., 2014). Proximal sensing has limitations involving portability and rapidity. In cotton, canopy height, reflectance, and temperature were measured simultaneously using a tractor modified with sensors (Andrade-Sanchez et al., 2014). Although this approach was accurate and more efficient than manual phenotyping, the time expenditure (0.84 ha hr^{-1}) was significant.

Remote sensing is defined as the process of measuring an object from a distance using a non-destructive and non-invasive approach (Araus and Cairns, 2014; Marshall et al., 2016). While this was initially done using manned aircrafts, unmanned aerial systems (UAS) are now used almost exclusively in agricultural research (Marshall et al., 2016). Unmanned aerial systems provide lower flight altitudes and higher spatial resolution (pixel size < 25cm), delivering more detailed image analysis (Wulder et al., 2004). Unmanned aerial systems are also able to cover entire experiments in a short time span, alleviating the time and portability limitations of proximal sensing (Ruixiu et al., 1989; Lan, 2009; Marshall et al., 2016).

Several types of sensors are used in the remote sensing of crops, but all are developed around the same principle of capturing the reflection and absorption of energy based on plant photosynthetically active tissue (Wiegand et al., 1986; Wanjura and Hatfield, 1987). Healthy plants absorb blue (~430nm) and red (~662nm) wavelengths through Chlorophyll A in the leaves. In Contrast , leaf reflectance is low on the electromagnetic spectrum except in the green wavelengths (~550nm) and throughout the infrared range (~700-1300nm) (Knipling, 1970). Indices similar to the normalized difference vegetation index (NDVI) and dark green color index

(DGCI) observe two or more spectral wavelengths, and respond to the amount of photosynthetically active tissue in the plant (Wiegand et al., 1986).

NDVI is the differenced ratio of reflectance in the red and near infrared wavelengths (Tucker, 1979), and has been used to evaluate many agronomic traits. DGCI was developed to measure the color of plants in digital images after it was discovered that the amount of red and blue light alters green color (Karcher and Richardson, 2003). This index has been used to quantify the intensity of leaf greenness for nitrogen content in corn (Karcher and Richardson, 2003) and turf (Rorie et al., 2011).

Although UASs can obtain high spatial resolution in comparison to satellite imaging, data collected from low altitude flights (30 m AGL) show that the relationship between remote sensing methods and ground evaluations improve with increasing target surface area (Haghighattalab et al., 2016; Duan et al., 2017). Remote sensing technologies must be amenable to the experimental design, including the plot size, in order to be effective in large breeding programs (Haghighattalab et al., 2016). Individual breeding programs have constraints in terms of space availability for research and budget, and there is a need for proof of concept research determining the ability of UAS technologies to replace or compliment manual methods of phenotyping. Given this, the objective of this research was to determine if plot size has a significant effect on the relationship between visual and proximal or remote sensing of stripe rust severity.

Materials and Methods

Germplasm

The germplasm used in this study consisted of 11 genotypes preselected from evaluations in 2017-2018 to represent the variability of the modified Cobb visual severity rating scale. The modified Cobb visual severity rating scale rates the percentage of leaf area infected from 0 to 100 in increments (0, 2, 7,15, 30, 50, 70, 85, 93, 98, 100), with 0 showing no sign of infection and 100 being the highest level of infection (Fig.1, Peterson et al., 1948). The 11 preselected genotypes included: ARGA06411-9-3-4 represented 100% severity, NC05-20671 at 98%, AR99263-7-1 at 93%, NC07-25169 at 85%, AR04015-5 at 70%, LA10191C-1 at 50%, TX13D5193 at 30%, AR06037-17-2 at 15%, ARLA07133C-3-4 at 7%, LA08115C-30 at 2% and AR00255-16-1 at 0% severity. In addition to the 11 preselected genotypes, two check cultivars were included, a resistant check, 'Pat' (Bacon et al., 2004) and susceptible check 'Croplan Genetics 514W' (CG514W), for a total of 13 lines.

Experimental Design

The experiment was conducted at the Milo J. Shult Agricultural Research and Extension Center in Fayetteville, Arkansas, during the 2018-2019 growing season. The 13 genotypes were drill-seeded in a split-plot design where plot-size was the whole-plot and genotype the was the split-plot factor, with genotype randomized for each plot size. Plots size included single-row (0.24 m width and 1.22 m length), two-row (0.50 m width and 1.22 m length), and four-row (1.21 m width and 1.22 m length). This design was replicated three times where each plot size contained all 13 genotypes (Fig.1).

The experiment was planted on October 23, 2018. Nitrogen fertilizer in the form of urea was applied after the tillering stage (Feekes 3-5) in two applications of 67 kg ha^{-1} and 33 kg ha^{-1}, respectively. Plots were rainfed and managed with Axial (Syngenta AG, Basel, CHE) for ryegrass, Harmony Xtra (DuPont Agroscienes, Wilmington, DE, USA) for winter annuals and Grizzly (Winfield United, Arden Hills, MN, USA) for aphids.

Stripe rust inoculation procedures ,visual and remote sensing evaluations, aerial platforms, active and passive sensors, flight parameters, and post flight processing procedures were identical to those in "CHAPTER 2: UTILITY OF UAS TO ASSESS STRIPE RUST SEVERITY AND DETECT KNOWN RESISTANCE GENES IN A SOFT RED WINTER WHEAT BREEDING NURSERY" (Jamison Murry[1], Richard Esten Mason, David Moon, Larry Purcell Leandro Mozzoni Dylan Larkin) regarding the experiment conducted in the second year.

Statistical Analysis

Each response variable was analyzed in an analysis of variance, and adjusted means were calculated using a mixed linear model in SAS 9.4 software (SAS Institute, Cary, NC):

$$Y_{ijk} = \mu + T_j + L_k + TL_{jk} + \beta_i + \square_{ijk}.$$

where Y_{ijk} is the response variables relative to the phenotypic observation, μ is the overall mean, T_j is the fixed plot size effect of the j^{th} treatment, L_k is the fixed genotype effect of the k^{th} genotype, TL_{jk} is the fixed plot size by genotype interaction effect, β_i is the random blocking effect of the i^{th} blocking variable, *and* $\square_{ijk}$ is the random error term. Linear regressions were used to determine the relationship between the visual and remote or proximal sensing data, among measurement days and by plot size in JMP Pro 14.2 software (SAS Institute, Cary, NC). The

coefficients of determination from the regression analysis were converted into Pearson correlation coefficients and transformed into Fisher's Z coefficients using the following formula:

$$z' = .5[\ln(1 + r) - \ln(1 - r)]$$

where ln is the natural log, and r is the correlation coefficient (Statistics How To, 2014). An online calculator (https://www.statisticshowto.datasciencecentral.com/fisher-z/) was then used to determine the significance between plot sizes using the z test statistic and the following formula:

$$Z_{observed} = (Z_1 - Z_2)\sqrt{\left(\frac{1}{N_1} - 3\right) + \left(\frac{1}{N_2} - 3\right)}$$

Where Z_1 and Z_2 are the converted r coefficients for comparisons, and N_1 and N_2 are the corresponding sample sizes (Statistics Solutions, 2019).

Results

Relationship Between DGCI and Visual Severity Ratings

The experiment had a mean visual severity rating of 20% at the booting stage, 30% at the heading stage, 40% at the grain-fill stage, and an AUDPC of 47, indicating positive disease progression. The effect of genotype was significant (p<0.0001) for all severity and DGCI measurements (Table 1). The effects of plot-size and the interaction of plot-size and genotype were significant for DGCI at grain-fill only. A significant linear relationship was observed between severity and DGCI across both days and all plot sizes. The strongest relationship observed between severity and DGCI was at the grain-fill stage for the four-row plot size (R^2 = 0.86, p<0.0001). In general, the relationship was strongest for the four-row (R^2 = 0.85 to 0.86) compared to the two-row (R^2= 0.72 to 0.71) and one-row (R^2 = 0.75 to 0.74) plot sizes (Table 2,

Fig. 2). However, comparing the correlation coefficients found no significant differences identified between plot size correlations across measurement days (Table 3).

Relationship Between UAS NDVI and Visual Severity Ratings

The effect of genotype was significant ($p<0.05$) for NDVI at booting. The effect of plot size and the interaction of plot size and genotype were not significant for NDVI (Table 1). The four-row plot size ($R^2 = 0.84$, $p< 0.0001$) had the strongest relationship between severity and NDVI, which was significantly different compared to the single-row ($R^2 = 0.02$, $p<0.6204$) but not the two-row ($R^2 = 0.78$, $p<0.0001$) plot sizes (Fig. 3, Table 2). The correlation coefficients for single-row and the two-row plot sizes were also significantly different from each other (Table 3).

Relationship Between Proximal NDVI and Visual Severity Ratings

The effect of genotype was significant ($p<0.0001$) for all proximal Greenseeker NDVI measurements (Table 1). The effect of plot size was significant ($p<0.05$) for the Greenseeker NDVI values at grain-fill only (Table 1). At the booting stage, the relationship between severity and proximal NDVI was greater for the four-row ($R^2 = 0.88$, $p<0.0001$) and two-row ($R^2 = 0.88$, $p<0.0001$), compared to the single-row ($R^2 = 0.86$, $p<0.0001$) plot size (Fig. 4, Table 2). At the grain-fill stage, the single-row ($R^2 = 0.98$, $p<0.0001$) plot size relationship was the strongest, followed by the four-row ($R^2 = 0.95$, $p<0.0001$) and two-row ($R^2 = 0.89$, $p<0.0001$), with no significant differences.

Relationship Between UAS and Proximal NDVI Measurements

The strongest relationship between proximal Greenseeker NDVI and remote NDVI occurred at the booting stage with the four-row plot size ($R^2 = 0.92$, $p< 0.0001$). but the four-row values were not significantly different from the two-row ($R^2 = 0.86$ $p<0.0001$). Both the two-row and

four-row were significantly greater than the single-row ($R^2 = 0.01$ $p<0.7862$) plot size relationship (Fig 5, Table 2 and 3

Discussion

When breeding field crops, plot sizes vary among field trials and generation of breeding lines, often contingent on breeding objectives, financial and land resources, and seed availability (Fehr, 1991). Smaller plots are mostly used in the early stages of breeding to evaluate genotypes rapidly and at lower cost (Fehr, 1991; Barmeier and Schmidhalter, 2016). When considering the use of UAS to phenotype large breeding nurseries in a heterogenous area, the spatial resolution to accurately capture differences in spectral reflectance for each plot must be considered (Lu and He, 2018). For stripe rust, the pixel size must be small enough to analyze disease symptoms. Increasing plot size can amplify the visibility of disease symptoms over the larger homogenous plot and increase ability to accurately determine severity.

Plot-Size Effect on the Relationship Between DGCI and Visual Assessments

The results of this study indicate that the relationship between visual severity and DGCI collected with a UAS was the strongest for the four-row plot sizes, though not significantly different from the two-row and one-row. The strong relationships among all the treatments and measurement days are likely attributed to the HSB transformation that DGCI utilizes, which is closely related to the human perception of color, evaluating the plots similarly to visual assessments. (Karcher and Richardson, 2003). Rorie et al (2011) showed that the greenness of corn and other non-legume crops is a strong indicator of nitrogen (N) status. They used DGCI to evaluate the N status of corn and found a strong relationship with SPAD units, a surrogate for N in crops. Stripe rust produces yellow-orange spores that induces leaf chlorosis similar to N

deficiency symptoms, resulting in the ability of DGCI to evaluate the symptoms of stripe rust across plot sizes.

It should be noted that for the two-row plot size, the susceptible check had a mean DGCI value that was higher than expected. The anticipated rating was a maximum mean of 0.60, similar to what was observed for CG514W in the single-row plot size, however as the plot size increased, the DGCI value slightly increased. Possible explanations include the stunting of growth for this specific genotype from disease severity, increased biomass of smaller vegetation captured within the polygon, or shading from neighboring genotypes, which could alter the DGCI value and classification of the genotype. Lu and He, (2018) showed that when classifying specific grass species in heterogeneous grasslands using a UAS, high spatial resolution flights (pixel size ≤5cm) captured shadowing effects and other vegetation, hindering the classification of desired species. With a pixel size of 1.8 cm, this effect was likely a cause of higher DGCI ratings observed for the susceptible CG514W genotype. Overall an increase in plot size did not significantly improve the relationship between visual and DGCI evaluations.

Plot Size Effect on the Relationship Between Visual Assessments and Multispectral NDVI

Similar to DGCI, the four-row plot size showed the strongest relationship between visual severity and remote NDVI, significantly equal to the two-row and significantly different from the single-row plot sizes. This difference is likely due to increased pixel count reducing the error associated with determining mean per plot NDVI. Devadas et al (2009) tested multiple vegetative indices in a controlled environment for ability to identify stripe rust against stem rust (*Puccinia graminis*) and leaf rust (*Puccinia triticina)* using a leaf reflectance spectrometer. The authors found that stripe rust produced the strongest response for many of the indices, including NDVI. Su et al (2018) evaluated the usefulness of a five-band multispectral camera (MicaSense

RedEdge) in the monitoring of stripe rust and found NDVI among the top three vegetative indices to discriminate stripe rust from healthy wheat plants at low altitude (26m). Statistical differences between plot sizes among the indices are likely attributed to the amplification of the stripe rust symptoms from the plot size increase and the ability of NDVI to better discriminate yellow rust from healthy biomass compared to DGCI.

Plot Size Effect on the Relationship Between Visual Severity and Proximal NDVI

Visual severity and Greenseeker NDVI were highly correlated across all plot sizes. The relationships did not show a statistical difference across plot sizes likely due to high resolution, limited atmospheric noise and simultaneous ratings of both visual and proximal evaluations. Since the Greenseeker evaluated each plot at 0.5 meters, the plot size was likely not a factor because each plot was analyzed individually, instead of multiple plots being evaluated at once like the elevated multispectral sensor, leading to no significant differences being detected. Arora et al (2013) visually and proximally evaluated stripe rust reactions four times at seven-day intervals, converting the visual ratings to area under the disease pressure curve (AUDPC) values. They observed a significant regression coefficient ($R^2 = 0.63$) between the AUDPC and NDVI and concluded that the ground based NDVI data could be effective in quantifying severity. Kumar et al (2015) used a hand-held Greenseeker NDVI sensor to map spot blotch disease resistance QTL in 108 germplasm lines and 335 single seed decent-derived lines from a cross of two wheat cultivars. They found significant relationships between proximal NDVI measurements and visual for both the single-seed-descent derived lines ($R^2 = 0.83$ $p<0.0001$) and the germplasm lines ($R^2 = 0.79$ $p<0.0001$). This evidence confirms the strong relationship between visual severity ratings and proximal sensing, and that proximal sensing can be used in phenotyping a large breeding population, preventing subjective ratings.

Plot Size Effect on the Relationship Between Proximal NDVI and Multispectral NDVI

The relationship between proximal and remote NDVI was significantly greater for the four-row and two-row plot sizes compared to the single-row. A reduction in spectral reflectance in small plots due to lower biomass in the sensor field of view and interference due to soil exposure have previously been reported (Barmeier and Schmidhalter, 2016). (Duan et al., 2017) used a large plot size (2m wide and 7m long) and observed a strong relationship between airborne multispectral NDVI and a handheld Greenseeker for both early ($R^2 = 0.85$ $p<0.01$) and late sowing dates ($R^2 = 0.84$, $p<0.01$) under variable irrigation, planting date, and nitrogen treatments. In contrast, (Haghighattalab et al., 2016) found only moderate correlation between red-edge NDVI and a handheld spectroradiometer ($R^2 =0.41$) for single-row plots under heat-stress. It should also be noted that the Greenseeker exhibited a larger range of NDVI values compared to the multispectral sensor. This 0.30-unit increase in range may be attributed to lower resolution at increased altitude of the multispectral sensor, making it incapable of sampling small patches of soil, increasing NDVI values with a smaller range, compared to the handheld Greenseeker. This observation was also made by (Duan et al., 2017).

Conclusion

Phenotyping is essential to cultivar development and new methods of higher throughput must be applicable across experimental designs. This research indicates that when using proximal or remote sensing to assess stripe rust severity, a larger plot size can significantly increase the relationship between visual and remote sensing measurements. The hand-held Greenseeker should also be considered for a more standardized and efficient method of phenotyping stripe rust severity. Further research is necessary to evaluate other indices in variable experimental designs and in more diverse germplasm.

Acknowledgments

We thank the Agriculture and Food Research Initiative Competitive Grant 2017-67007-25939 (Wheat-CAP) from the USDA National Institute of Food and Agriculture, the Arkansas Wheat Promotion Board, and the USDA Wheat and Barley Stripe Rust Initiative for financial support; Dr. L. Mozzoni, Dr. L. Purcell, and Mr. Daniel Rogers for their assistance in providing the UASs and remote sensors used in this study.

Refereneces

Andrade-Sanchez, P., M.A. Gore, J.T. Heun, K.R. Thorp, A.E. Carmo-Silva, et al. 2014. Development and evaluation of a field-based high-throughput phenotyping platform. Functional Plant Biol. 41(1): 68–79. doi: 10.1071/FP13126.

Araus, J.L., and J.E. Cairns. 2014. Field high-throughput phenotyping: the new crop breeding frontier. Trends in Plant Science 19(1): 52–61. doi: 10.1016/j.tplants.2013.09.008.

Arora, A., R.K. Sharma, M.S. Saharan, K. Venkatesh, N. Dilbaghi, et al. 2013. Quantifying stripe rust reactions in wheat using a handheld NDVI remote sensor. Proceedings of BGRI2013 Technical Workshop. p. 19–22

Bacon, R.K., J.T. Kelly, E.A. Milus, and C.E. Parsons. 2004. Registration of'Pat'wheat. Crop science 44(2): 694–696.

Barmeier, G., and U. Schmidhalter. 2016. High-throughput phenotyping of wheat and barley plants grown in single or few rows in small plots using active and passive spectral proximal sensing. Sensors 16(11): 1860. doi: 10.3390/s16111860.

Brachi, B., G.P. Morris, and J.O. Borevitz. 2011. Genome-wide association studies in plants: the missing heritability is in the field. Genome Biology 12(10): 232. doi: 10.1186/gb-2011-12-10-232.

Carleton, M.A. 1915. Hard wheats winning their way. US Department of Agriculture.

Chen, X.M. 2005. Epidemiology and control of stripe rust [*Puccinia striiformis* f. sp. *tritici*] on wheat. Canadian Journal of Plant Pathology 27(3): 314–337. doi: 10.1080/07060660509507230.

Chen, X.M. 2007. Challenges and solutions for stripe rust control in the United States. Australian Journal of Agricultural Research 58(6): 648–655.

Chen, X., M. Moore, E.A. Milus, D.L. Long, R.F. Line, et al. 2002. Wheat stripe rust epidemics and races of Puccinia striiformis f. sp. Tritici in the United States in 2000. Plant Disease 86(1): 39–46. doi: 10.1094/PDIS.2002.86.1.39.

Chen, X., L. Penman, A. Wan, and P. Cheng. 2010. Virulence races of Puccinia striiformis f. sp. tritici in 2006 and 2007 and development of wheat stripe rust and distributions, dynamics, and evolutionary relationships of races from 2000 to 2007 in the United States. Canadian Journal of Plant Pathology 32(3): 315–333. doi: 10.1080/07060661.2010.499271.

Devadas, R., D.W. Lamb, S. Simpfendorfer, and D. Backhouse. 2009. Evaluating ten spectral vegetation indices for identifying rust infection in individual wheat leaves. Precision Agriculture; Dordrecht 10(6): 459–470. doi: http://0-dx.doi.org.library.uark.edu/10.1007/s11119-008-9100-2.

Duan, T., S.C. Chapman, Y. Guo, and B. Zheng. 2017. Dynamic monitoring of NDVI in wheat agronomy and breeding trials using an unmanned aerial vehicle. Field Crops Research 210: 71–80.

Fehr, W. 1991. Principles of cultivar development: theory and technique. Macmillian Publishing Company.

Furbank, R.T., and M. Tester. 2011. Phenomics – technologies to relieve the phenotyping bottleneck. Trends in Plant Science 16(12): 635–644. doi: 10.1016/j.tplants.2011.09.005.

Haghighattalab, A., L.G. Perez, S. Mondal, D. Singh, D. Schinstock, et al. 2016. Application of unmanned aerial systems for high throughput phenotyping of large wheat breeding nurseries. Plant Methods; London 12. doi: http://0-dx.doi.org.library.uark.edu/10.1186/s13007-016-0134-6.

Jannink, J.-L., A.J. Lorenz, and H. Iwata. 2010. Genomic selection in plant breeding: from theory to practice. Brief Funct Genomics 9(2): 166–177. doi: 10.1093/bfgp/elq001.

Karcher, D.E., and M.D. Richardson. 2003. Quantifying turfgrass color using digital image analysis. Crop Science 43(3): 943–951. doi: 10.2135/cropsci2003.9430.

Knipling, E.B. 1970. Physical and physiological basis for the reflectance of visible and near-infrared radiation from vegetation. Remote sensing of environment 1(3): 155–159.

Kumar, V., A. Singh, S.A. Mithra, S.L. Krishnamurthy, S.K. Parida, et al. 2015. Genome-wide association mapping of salinity tolerance in rice (Oryza sativa). DNA research 22(2): 133–145.

Lan, Y. 2009. Development of an integration sensor and instrumentation system for measuring crop conditions. Agricultural Engineering International: CIGR Journal.

Line, R.F. 2002. Stripe rust of wheat and barley in North America: A retrospective historical review. Annual Review of Phytopathology; Palo Alto 40: 75.

Lu, B., and Y. He. 2018. Optimal spatial resolution of Unmanned Aerial Vehicle (UAV)-acquired imagery for species classification in a heterogeneous grassland ecosystem. GIScience & Remote Sensing 55(2): 205–220. doi: 10.1080/15481603.2017.1408930.

Marshall, D.M., R.K. Barnhart, S.B. Hottman, E. Shappee, and M.T. Most. 2016. Introduction to unmanned aircraft systems. Crc Press.

Peterson, R.F., A.B. Campbell, and A.E. Hannah. 1948. A diagrammatic scale for estimating rust intensity on leaves and stems of cereals. Canadian journal of research 26(5): 496–500.

Poland, J., and K. Price. 2015. Plant high-throughput phenotyping using photogrammetry and 3D modeling techniques.

Rorie, R.L., L.C. Purcell, D.E. Karcher, and C.A. King. 2011a. The Assessment of leaf nitrogen in corn from digital images. Crop Science 51(5): 2174–2180. doi: 10.2135/cropsci2010.12.0699.

Rorie, R.L., L.C. Purcell, M. Mozaffari, D.E. Karcher, C.A. King, et al. 2011b. Association of "greenness" in corn with yield and leaf nitrogen concentration. Agronomy Journal; Madison 103(2): 529–535.

Ruixiu, S., J.B. Wilkerson, L.R. Wilhelm, and F.D. Tompkins. 1989. A microcomputer-based morphometer for bush-type plants. Computers and Electronics in Agriculture 4(1): 43–58. doi: 10.1016/0168-1699(89)90013-6.

Statistics How To. 2014. Fisher Z -Transformation. Statistics How To. https://www.statisticshowto.datasciencecentral.com/fisher-z/ (accessed 10 January 2020).

Statistics Solutions. 2019. Comparing Correlation Coefficients. Statistics Solutions. https://www.statisticssolutions.com/comparing-correlation-coefficients/ (accessed 10 January 2020).

Stubbs, R.W. 1985. 3 - Stripe Rust. In: Roelfs, A.P. and Bushnell, W.R., editors, Diseases, Distribution, Epidemiology, and Control. Academic Press. p. 61–101

Su, J., C. Liu, M. Coombes, X. Hu, C. Wang, et al. 2018. Wheat yellow rust monitoring by learning from multispectral UAV aerial imagery. Computers and Electronics in Agriculture 155: 157–166. doi: 10.1016/j.compag.2018.10.017.

Wanjura, D.F., and J.L. Hatfield. 1987. Sensitivity of spectral vegetative indices to crop biomass. Transactions of the ASAE 30(3): 810–0816.

Wegulo, S.N., and E. Byamukama. 2012. Rust Diseases of Wheat. NebGuide, University of Nebraska- Lincoln (Plant Disease Wheat). http://extensionpublications.unl.edu/assets/html/g2180/build/g2180.htm#target4 (accessed 9 July 2019).

White, J.W., P. Andrade-Sanchez, M.A. Gore, K.F. Bronson, T.A. Coffelt, et al. 2012. Field-based phenomics for plant genetics research. Field Crops Research 133: 101–112. doi: 10.1016/j.fcr.2012.04.003.

Wiegand, C.L., A.J. Richardson, and P.R. Nixon. 1986. Spectral components analysis: a bridge between spectral observations and agrometeorological crop models. IEEE transactions on geoscience and remote sensing (1): 83–89.

Wulder, M.A., R.J. Hall, N.C. Coops, and S.E. Franklin. 2004. High spatial resolution remotely sensed data for ecosystem characterization. BioScience 54(6): 511–521. doi: 10.1641/0006-3568(2004)054[0511:HSRRSD]2.0.CO;2.

Tables and Figures

Table 1. Analysis of variance for stripe rust severity, proximal, and remote measurements in 13 wheat genotypes evaluated in 2018-2019 in inoculated nursery in Fayetteville, AR.

	P-value		
Trait and Growth Stage	**Genotype**	**Plot Size**	**Genotype by Plot Size**
Severity at booting	<0.0001	0.6248	0.3786
Severity at heading	<0.0001	0.8527	0.9163
Severity at grain-fill	<0.0001	0.2136	0.2887
DGCI at booting	<0.0001	0.0590	0.2193
DGCI at grain-fill	<0.0001	<0.0001	0.0097
NDVI at booting	0.0418	0.3469	0.4812
Greenseeker at booting	<0.0001	0.0636	0.1500
Greenseeker at heading	<0.0001	0.0467	0.8606
Greenseeker at grain-fill	<0.0001	0.4736	0.5768

Table 2. Linear Regressions for stripe rust severity, proximal, and remote measurements in 13 wheat genotypes evaluated in 2018-2019 in inoculated nursery in Fayetteville, AR.

Plot Size	Regression	R^2	r	P-value
Single-row	Severity x DGCI at booting	0.75	0.87	<0.0001
	Severity x DGCI at grain-fill	0.74	0.86	0.0002
	Severity x NDVI at booting	0.02	0.14	0.6204
	Severity x Greenseeker at booting	0.86	0.93	<0.0001
	Severity x Greenseeker at grain-fill	0.98	0.99	<0.0001
	NDVI x Greenseeker at booting	0.01	0.10	0.7862
Two-row	Severity x DGCI at booting	0.72	0.85	0.0002
	Severity x DGCI at grain-fill	0.71	0.84	0.0032
	Severity x NDVI at booting	0.78	0.88	<0.0001
	Severity x Greenseeker at booting	0.88	0.94	<0.0001
	Severity x Greenseeker at grain-fill	0.89	0.94	<0.0001
	NDVI x Greenseeker at booting	0.86	0.93	<0.0001
Four-row	Severity x DGCI at booting	0.85	0.92	<0.0001
	Severity x DGCI at grain-fill	0.86	0.93	<0.0001
	Severity x NDVI at booting	0.84	0.92	<0.0001
	Severity x Greenseeker at booting	0.88	0.93	<0.0001
	Severity x Greeseeker at grain-fill	0.95	0.97	<0.0001
	NDVI x Greenseeker at booting	0.92	0.95	<0.0001

Table 3. Fisher's Z-test of the correlation coefficients over plot sizes for stripe rust severity, Greenseeker, and UAS relationships

Relationship	Plot-size Comparison	Z Statistic	P-value
Severity x DGCI at booting	1-row x 2-row	0.17	0.865
	1-row x 4-row	0.57	0.568
	2-row x 4-row	0.74	0.459
Severity x DGCI at grain-fill	1-row x 2-row	0.16	0.873
	1-row x 4-row	0.82	0.412
	2-row x 4-row	0.79	0.429
Severity x NDVI at booting	1-row x 2-row	2.76	0.006
	1-row x 4-row	3.24	0.001
	2-row x 4-row	0.48	0.631
Severity x Greenseeker at booting	1-row x 2-row	0.18	0.857
	1-row x 4-row	0	1
	2-row x 4-row	0.18	0.857
Severity x Greenseeker at grain-fill	1-row x 2-row	2.03	0.042
	1-row x 4-row	1.24	0.215
	2-row x 4-row	0.79	0.429
NDVI x Greenseeker at booting	1-row x 2-row	3.48	0.001
	1-row x 4-row	3.87	<0.001
	2-row x 4-row	0.39	0.696

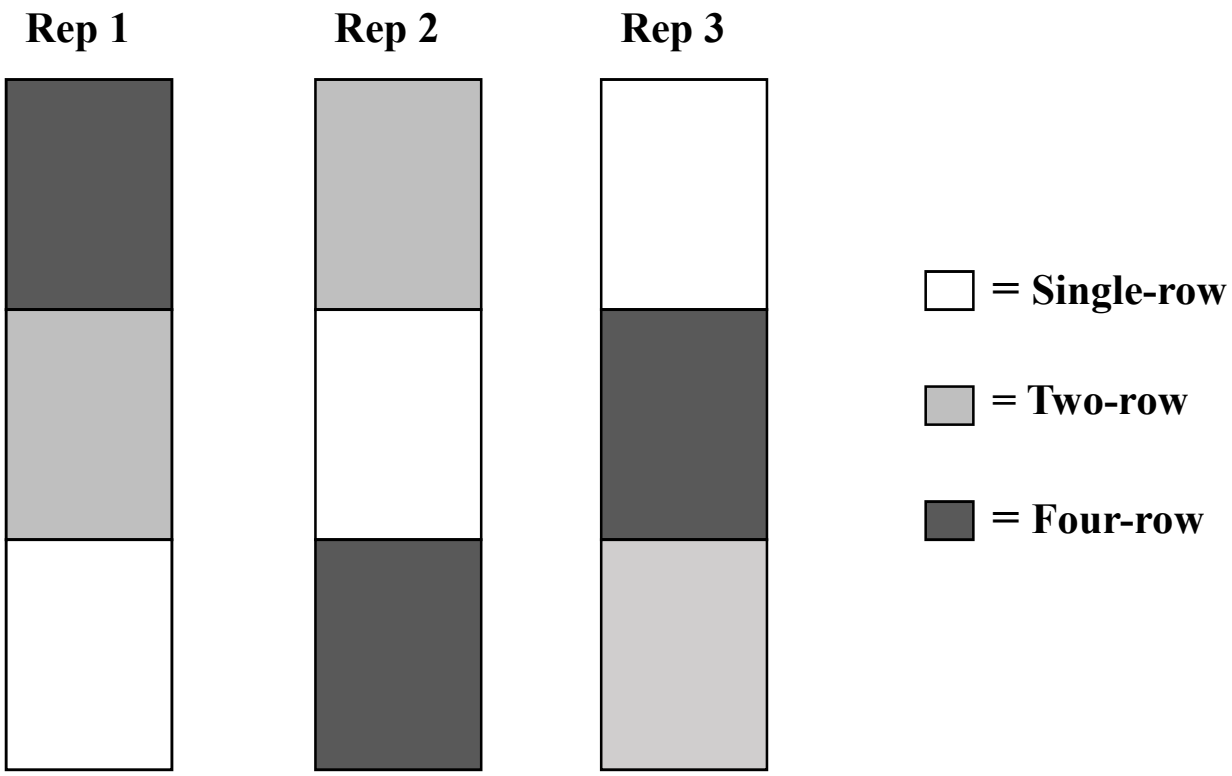

Figure 1: Field design of the genotypes planted it each plot size, respectively, planted in three replications.

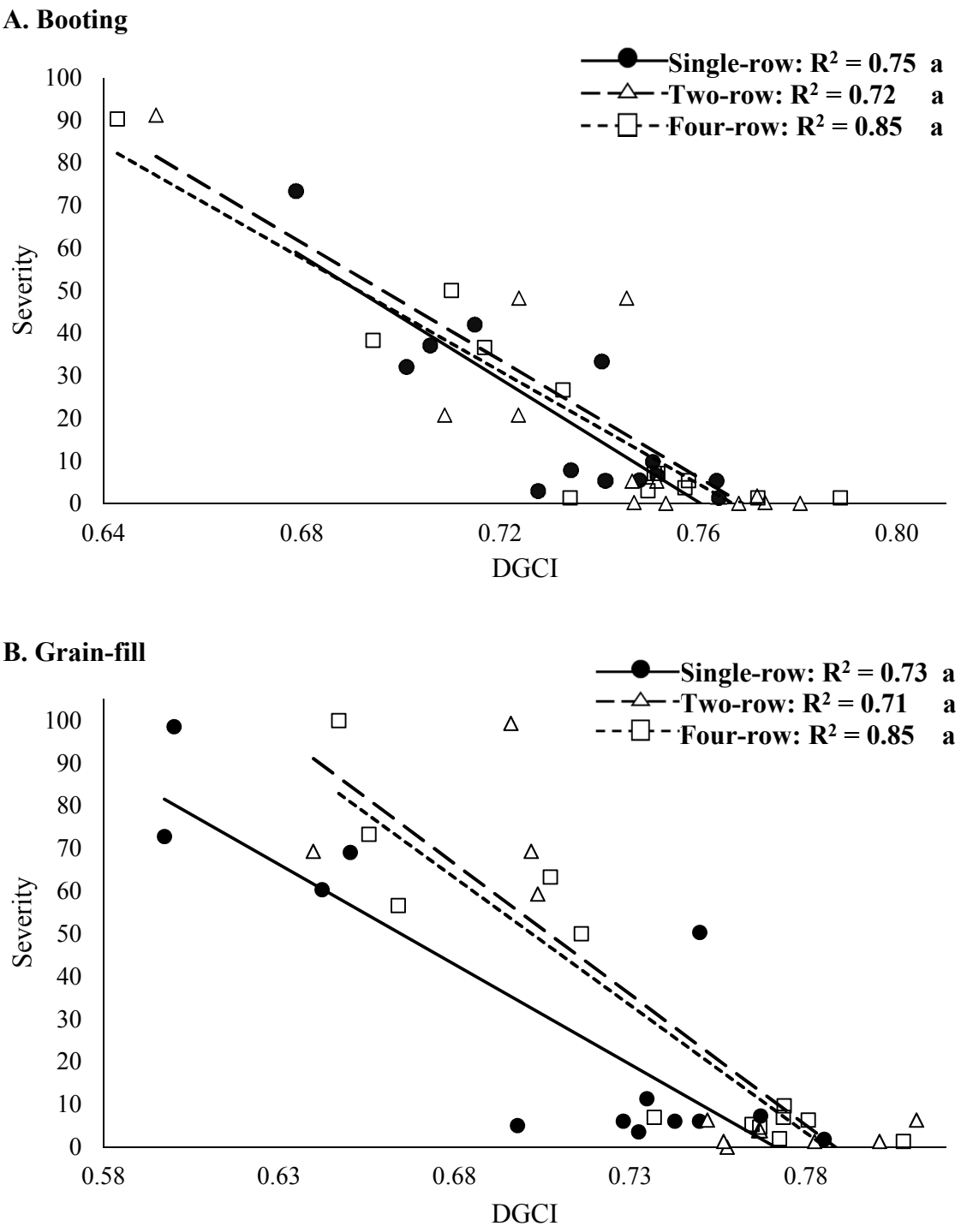

Figure 2: Linear relationships between visual stripe rust severity and dark green color index (DGCI) for 13 wheat lines in single-row, two-row, and four-row plots at the (A) Booting stage and (B) Grain-fill stage. Relationships with the same letters are not significantly different from each other (Fisher's Z-test)

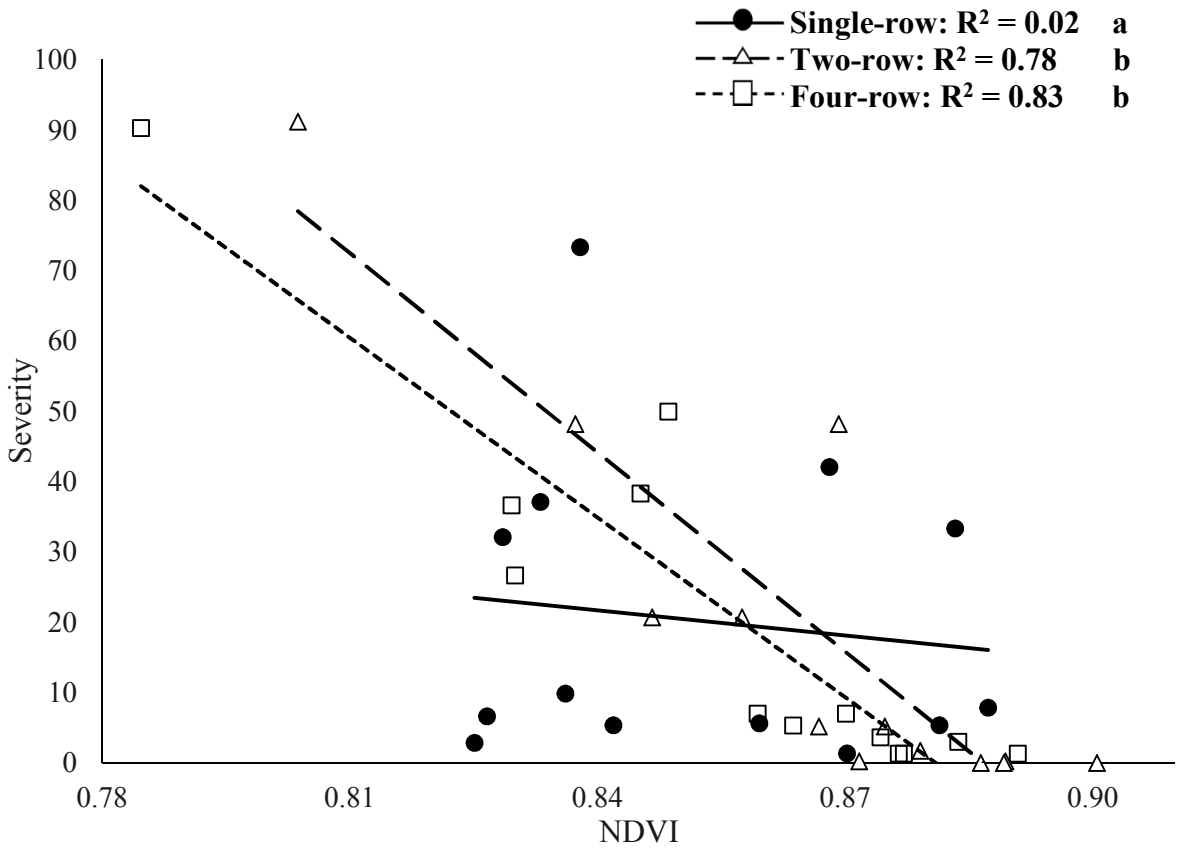

Figure 3: Linear relationships between visual stripe rust severity and multispectral NDVI for 13 wheat lines in single-row, two-row, and four-row plots at the booting stage. Relationships with the same letters are not significantly different from each other (Fisher's Z-test)

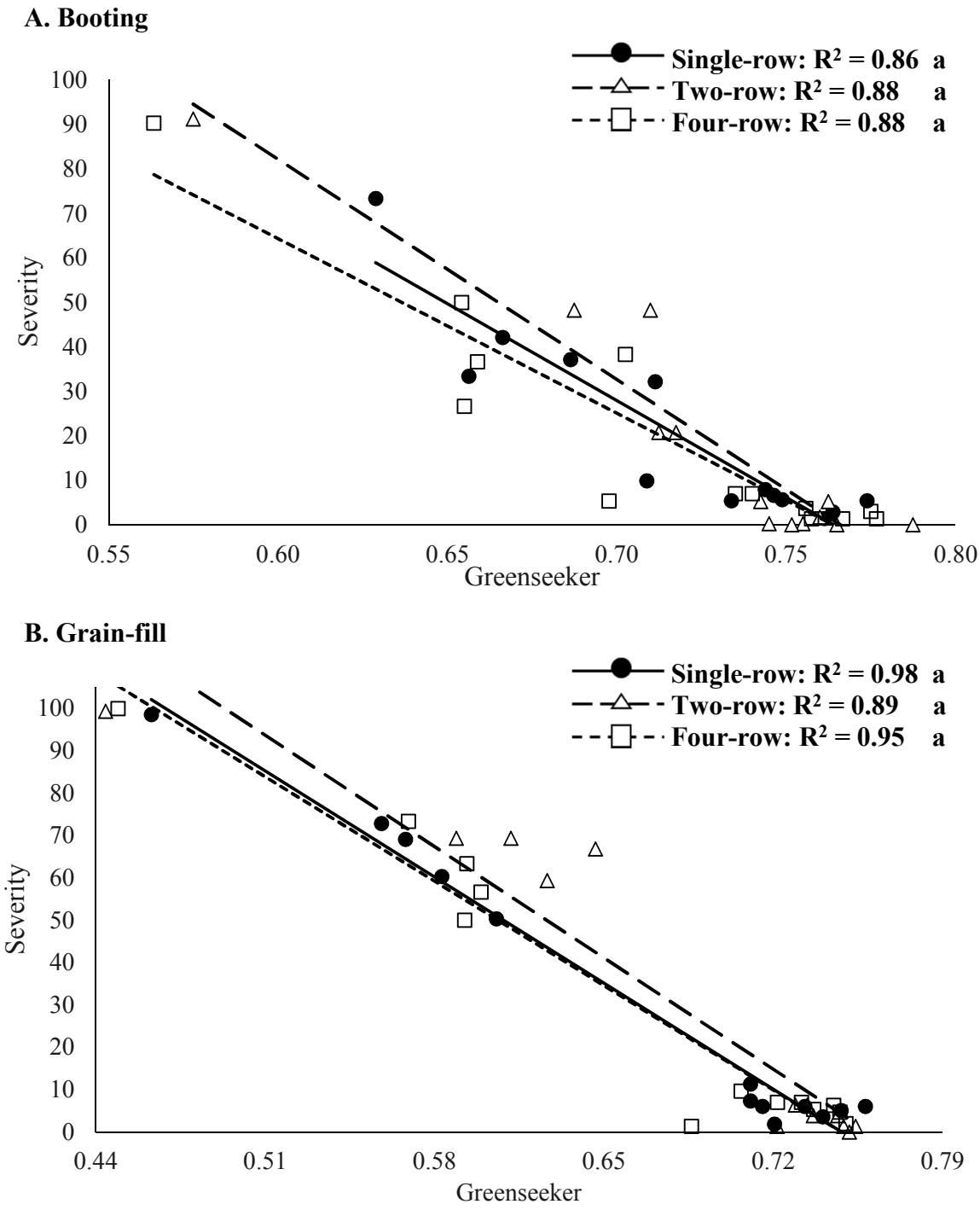

Figure 4: Linear relationships between visual stripe rust severity and proximal Greenseeker NDVI for 13 wheat lines in single-row, two-row, and four-row plot sizes at the (A) Booting stage and (B) Grain-fill stage. Relationships with the same letters are not significantly different from each other (Fisher's Z-test)

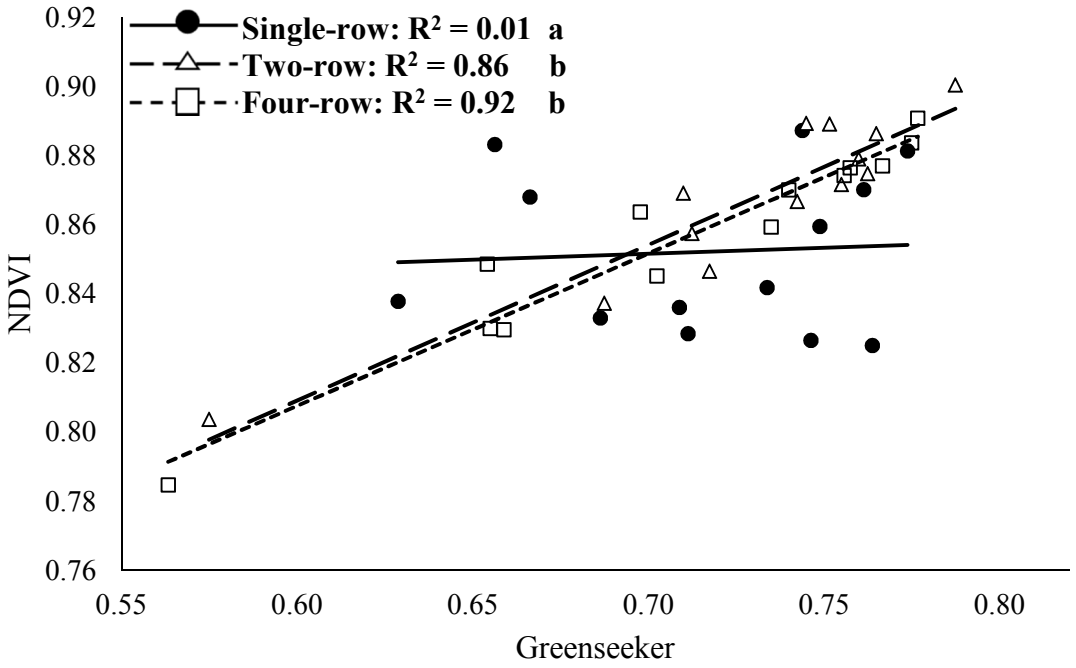

Figure 5: Linear relationships between proximal Greenseeker NDVI and multispectral NDVI for 13 wheat lines in single-row, two-row, and four-row at the booting stage. Relationships with the same letters are not significantly different from each other (Fisher's Z-test)